The Astrophysical Journal, 966:199 (16pp), 2024 May 10 https://doi.org/10.3847/1538-4357/ad3758

Dramatic Rebrightening of the Type-changing Stripped-envelope Supernova SN 2023aew

Yashvi Sharma[1], Jesper Sollerman[2], Shrinivas R. Kulkarni[1], Takashi J. Moriya[3,4,5], Steve Schulze[6], Stan Barmentloo[2], Michael Fausnaugh[7], Avishay Gal-Yam[8], Anders Jerkstrand[2], Tomás Ahumada[1], Eric C. Bellm[9], Kaustav K. Das[1], Andrew Drake[1], Christoffer Fremling[1], David Hale[10], Saarah Hall[6], K. R. Hinds[11], Theophile Jegou du Laz[1], Viraj Karambelkar[1], Mansi M. Kasliwal[1], Frank J. Masci[12], Adam A. Miller[6], Guy Nir[13], Daniel A. Perley[11], Josiah N. Purdum[10], Yu-Jing Qin[1], Nabeel Rehemtulla[6,14], R. Michael Rich[15], Reed L. Riddle[10], Antonio C. Rodriguez[1], Sam Rose[1], Jean Somalwar[1], Jacob L. Wise[11], Avery Wold[12], Lin Yan[1], and Yuhan Yao[16,17]

[1] Division of Physics, Mathematics and Astronomy, California Institute of Technology, Pasadena, CA 91125, USA; yssharma@astro.caltech.edu
[2] Department of Astronomy, The Oskar Klein Center, Stockholm University, AlbaNova, 10691 Stockholm, Sweden
[3] National Astronomical Observatory of Japan, National Institutes of Natural Sciences, 2-21-1 Osawa, Mitaka, Tokyo 181-8588, Japan
[4] Graduate Institute for Advanced Studies, SOKENDAI, 2-21-1 Osawa, Mitaka, Tokyo 181-8588, Japan
[5] School of Physics and Astronomy, Monash University, Clayton, Victoria 3800, Australia
[6] Center for Interdisciplinary Exploration and Research in Astrophysics (CIERA), Northwestern University, 1800 Sherman Avenue, Evanston, IL 60201, USA
[7] Department of Physics & Astronomy, Texas Tech University, Lubbock, TX 79410-1051, USA
[8] Department of Particle Physics and Astrophysics, Weizmann Institute of Science, 234 Herzl Street, 76100 Rehovot, Israel
[9] DIRAC Institute, Department of Astronomy, University of Washington, 3910 15th Avenue NE, Seattle, WA 98195, USA
[10] Caltech Optical Observatories, California Institute of Technology, Pasadena, CA 91125, USA
[11] Astrophysics Research Institute, Liverpool John Moores University, Liverpool Science Park, 146 Brownlow Hill, Liverpool L3 5RF, UK
[12] IPAC, California Institute of Technology, 1200 E. California Boulevard, Pasadena, CA 91125, USA
[13] Department of Astronomy, University of California, Berkeley, CA 94720-3411, USA
[14] Department of Physics and Astronomy, Northwestern University, 2145 Sheridan Road, Evanston, IL 60208, USA
[15] UCLA Dept of Physics and Astronomy, PAB 430 Portola Plaza, Box 951547, Los Angeles, CA 90095-1547, USA
[16] Miller Institute for Basic Research in Science, 468 Donner Lab, Berkeley, CA 94720, USA
[17] Department of Astronomy, University of California, Berkeley, CA 94720, USA
Received 2024 February 10; revised 2024 March 21; accepted 2024 March 23; published 2024 May 8

Abstract

Multipeaked supernovae with precursors, dramatic light-curve rebrightenings, and spectral transformation are rare, but are being discovered in increasing numbers by modern night-sky transient surveys like the Zwicky Transient Facility. Here, we present the observations and analysis of SN 2023aew, which showed a dramatic increase in brightness following an initial luminous (−17.4 mag) and long (∼100 days) unusual first peak (possibly precursor). SN 2023aew was classified as a Type IIb supernova during the first peak but changed its type to resemble a stripped-envelope supernova (SESN) after the marked rebrightening. We present comparisons of SN 2023aew's spectral evolution with SESN subtypes and argue that it is similar to SNe Ibc during its main peak. P-Cygni Balmer lines are present during the first peak, but vanish during the second peak's photospheric phase, before Hα resurfaces again during the nebular phase. The nebular lines ([O I], [Ca II], Mg I], Hα) exhibit a double-peaked structure that hints toward a clumpy or nonspherical ejecta. We analyze the second peak in the light curve of SN 2023aew and find it to be broader than that of normal SESNe as well as requiring a very high ^{56}Ni mass to power the peak luminosity. We discuss the possible origins of SN 2023aew including an eruption scenario where a part of the envelope is ejected during the first peak and also powers the second peak of the light curve through interaction of the SN with the circumstellar medium.

Unified Astronomy Thesaurus concepts: Core-collapse supernovae (304); Type Ib supernovae (1729); Type Ic supernovae (1730)

Supporting material: machine-readable tables

1. Introduction

Core-collapse (CC) supernovae (SNe) mark the final explosions of massive stars ($\gtrsim 8\,M_{\odot}$), and stripped-envelope SNe (SESNe) represent CC in stars that have lost most—or all—of their envelopes prior to explosion. This includes Type IIb SNe (some H left), SNe Ib (no H, some He), and SNe Ic (neither H nor He; Gal-Yam 2017).

Even though we now have hundreds of well-observed SESNe, there are still several open questions regarding their nature, when it comes to both their progenitor stars and their powering mechanism. Binarity seems to be a key component for stripping their envelopes, with arguments supported by relatively low ejecta masses, large relative rates (Smith 2011), and direct evidence of a binary system after the SESN 2022jli (Chen et al. 2024). These deduced ejecta masses often come from comparisons with simple analytical models (e.g., Arnett 1982; Barbarino et al. 2021; Yang & Sollerman 2023), which match reasonably well with the observed light curves assuming powering by radioactive ^{56}Ni. However, modern explosion models are unable to produce the amount of radioactive nickel required for the brighter Type Ibc SNe (Sollerman et al. 2022), and some SESNe show light-curve features that are not compatible with the standard scenario. Such unusual SESNe have emerged from the large samples of SNe now

available and include double-bump light curves (LCs), for example for SN 2019cad (Gutiérrez et al. 2021), SN 2022xxf (Kuncarayakti et al. 2023), and SN 2022jli (Chen et al. 2024), where different powering mechanisms were suggested in each of these cases for explaining the second LC bump.

In this paper we present the unusual stripped-envelope SN 2023aew (ZTF23aaawbsc) discovered as part of the Zwicky Transient Facility Bright Transient Survey (BTS; Fremling et al. 2020; Perley et al. 2020; Rehemtulla et al. 2024). This supernova shows an unprecedented first peak with a broad light curve and a slight plateau followed by another unusually broad light curve for the second peak. Spectrally, this object is clearly an SESN, but it is unlike any previous such objects.

The paper is organized as follows. In Section 2 we present the discovery and the observations of our SN, as well as details about the data reductions and calibrations. Section 3 presents an analysis of the photometric and spectroscopic data as well as comparisons to a number of similar SNe from the literature. In Section 4 we discuss in particular the mechanisms that could power the main light-curve peak of SN 2023aew, and in this connection we also present a few other objects with relevant observations. Finally, Section 5 presents our conclusions and a short discussion where we put our results in context.

2. Observations

In this section, we present our observations of SN 2023aew obtained over 300 days with multiple instruments and describe the data processing methods.

2.1. Discovery

SN 2023aew was detected in Zwicky Transient Facility (ZTF; Bellm et al. 2019; Graham et al. 2019; Dekany et al. 2020) data obtained with the Palomar Schmidt 48 inch Samuel Oschin telescope (P48) on 2023 January 23 (MJD 59967.511) and the discovery was reported to the Transient Name Server (TNS[18]) by ALeRCE (Förster et al. 2021; Munoz-Arancibia et al. 2023). This first ZTF detection magnitude was 18.05 in the r band at the J2000.0 coordinates $\alpha = 17^{\rm h}40^{\rm m}51\overset{\rm s}{.}395$, $\delta = +66°12'22\overset{''}{.}62$. The transient is apparently positioned in the outskirts of the spiral host galaxy SDSS J174050.55 +661220.7. The transient was subsequently reported to TNS by Gaia (Hodgkin et al. 2021) in February, by ATLAS (Tonry et al. 2018) in March, and by MASTER (Lipunov et al. 2019) in May when it began to brighten again. Gaia reported an 18.16 mag detection in the Gaia G band two days before the ZTF discovery (i.e., at MJD 59965.284). The last 3σ upper limit is ∼200 days before first detection in the ATLAS o band and ∼500 days before first detection in the ZTF r band. However, the Transiting Exoplanet Survey Satellite (TESS; Ricker 2014) had a serendipitous two months of coverage of SN 2023aew right before the ZTF discovery (from MJD 59910 to 59962). TESS captured a slow, 30 days rise of this SN whereas ground-based telescopes only caught the tail of this transient at its ZTF discovery (see Figure 1). We derive an explosion epoch of MJD 59936.18 ± 1.4 days by fitting a power law to an 8 hr binned TESS-Red band light curve (details in Section 2.3; Fausnaugh et al. 2021). Therefore, all phases throughout this paper will be reported with respect to this estimate of the explosion epoch.

[18] https://www.wis-tns.org

The transient was spectroscopically classified as an SN IIb by ZTF (Wise et al. 2023) on 2023 January 27 (4 days after ZTF discovery) with a spectrum obtained using the Spectral Energy Distribution Machine (SEDM; Ben-Ami et al. 2012; Blagorodnova et al. 2018) on the Palomar 60 inch telescope (P60; Cenko et al. 2006) and its `superfit` (Howell et al. 2005) match to SN IIb templates at a redshift of $z = 0.025$. This is consistent with the redshift of $z = 0.0255 \pm 0.0001$ obtained from the narrowest lines in our late, high signal-to-noise ratio Keck II/ESI spectrum (Section 2.3). Using a flat cosmology with $H_0 = 70$ km s^{-1} Mpc^{-1} and $\Omega_m = 0.3$, this redshift corresponds to a luminosity distance of 111 Mpc. The transient, initially classified as SN IIb, was observed to have a smooth initial light-curve decline for ∼25 days, which then turned into a slow plateau for another ∼50 days in ground-based optical data. The great surprise came with the rapid rebrightening of SN 2023aew, which started around 2023 April 11 (MJD 60045), wherein the SN rose by ∼2 mag in ∼10 days. As spectroscopic campaigns began in earnest, Frohmaier et al. (2023) reported their spectrum taken on 2023 April 20 with SPRAT (Piascik et al. 2014) on the Liverpool Telescope (LT; Steele et al. 2004) to be consistent with SN Ib templates albeit at a slightly higher redshift using SNID (Blondin & Tonry 2007). Hoogendam et al. (2023) reported three more spectra taken with SNIFS on the University of Hawaii 2.2 m telescope on 2023 April 23, April 25, and April 29, which were more consistent with late-time SN Ic templates.

2.2. Optical Photometry

We obtained forced point-spread function photometry via the ZTF forced photometry service (Masci et al. 2019, 2023; IRSA 2022) in g, r, and i bands and via ATLAS forced photometry service (Tonry et al. 2018; Smith et al. 2020) in c and o bands. Additional photometry was obtained with the Rainbow camera on P60 and processed with the automatic image subtraction pipeline `FPipe` (Fremling et al. 2016), and with the Optical wide field camera (IO:O) on LT (Steele et al. 2004). The Gaia G-band photometry was obtained from Gaia Alerts service.[19] All photometry is corrected for Milky Way (MW) extinction using the Python package `extinction` (Barbary 2016), the dust extinction law from Fitzpatrick (1999), the Schlafly & Finkbeiner (2011) dust map, $E(B-V) = 0.0386$ mag, and R_V of 3.1. All measurements are converted into flux units for the analysis. We do not account for the host reddening given the transient is in the outskirts of the host galaxy. The optical photometry is included in Table 6.

2.3. TESS Photometry

SN 2023aew had serendipitous coverage from TESS observations of Sector 59 and 60 from MJD 59910 to 59962—two months before the first ZTF detection. The TESS-Red[20] filter extends from 5802.57 to 11171.45 Å with a reference wavelength of 7697.60 Å. Image subtraction and forced photometry at SN 2023aew's location were carried out according to the methodology in Fausnaugh et al. (2021). The differential flux has a cadence of 200 s but was binned into 6 hr bins and converted into Vega magnitudes. These were further converted to the AB system and corrected for MW

[19] http://gsaweb.ast.cam.ac.uk/alerts/home

[20] http://svo2.cab.inta-csic.es/theory/fps/index.php?mode=browse&gname=TESS&asttype=

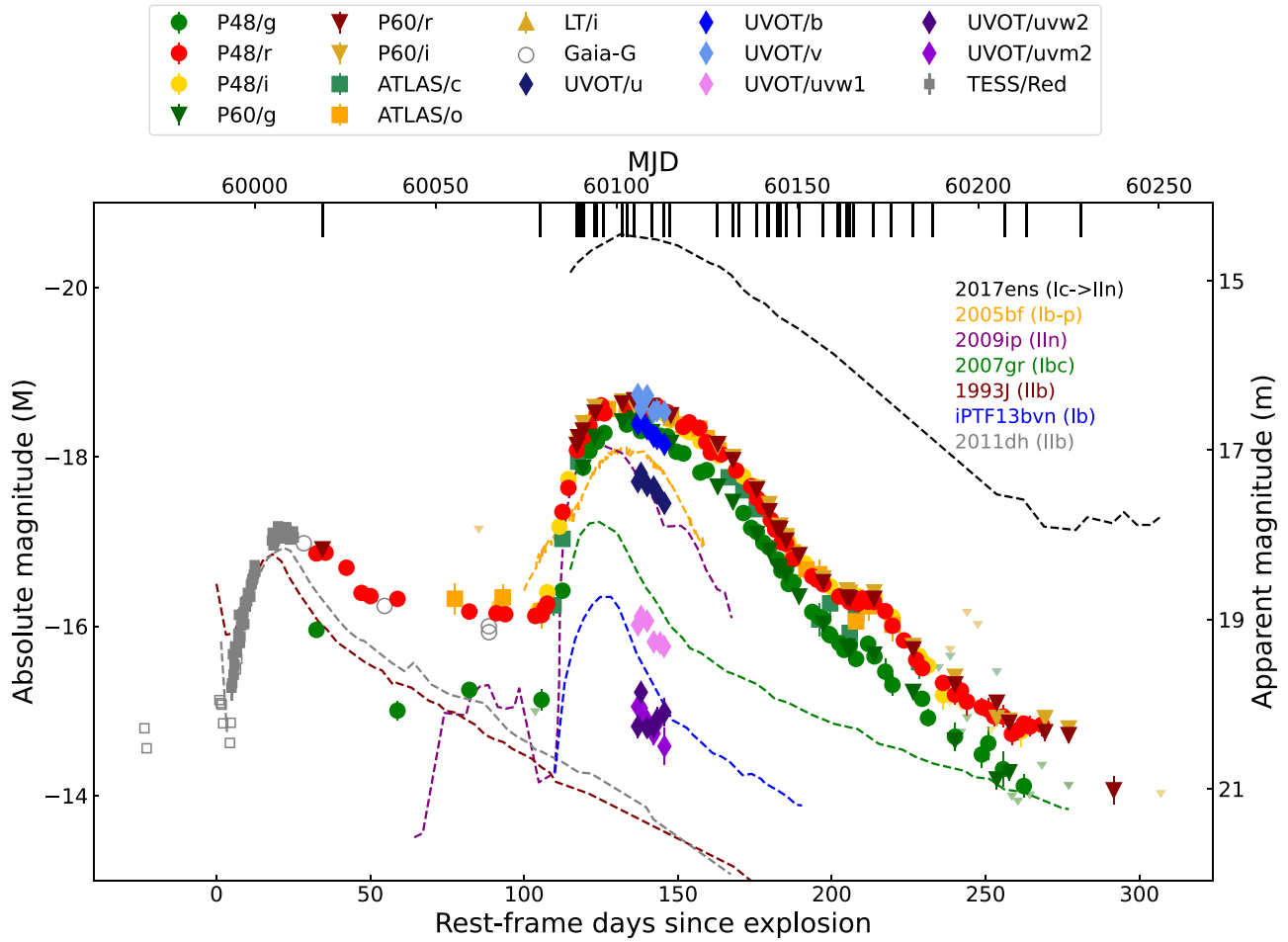

Figure 1. Light curve of SN 2023aew. The TESS observations cover the rise of the first peak and are shown as gray squares, with 5σ significance denoted with full markers and 3σ with empty markers. The spectroscopic epochs are marked with black lines at the top. Also shown for comparison are absolute magnitude *r*-band light curves of SNe 1993J (IIb), 2011dh (IIb), 2005bf (Ib-pec), 2007gr (Ic), 2009ip (IIn), iPTF13bvn (Ib), and the type-changing 2017ens (Ic to IIn). SNe 1993J and 2011dh are shifted to match their first detection with the explosion epoch of SN 2023aew. Other comparison SNe are shifted by ∼100 days to match the start of the second peak. The overall light-curve shape is somewhat similar to that of SN 2009ip but is broader, with the second peak having similar broadness to SN 2017ens.

extinction following the method in the previous section and using the TESS-Red reference wavelength. The binned TESS photometry is included in Table 3.

2.4. Swift Ultraviolet/Optical Telescope Photometry

The field was observed with the Ultraviolet/Optical Telescope (UVOT; Roming et al. 2005) aboard the Swift satellite (Gehrels et al. 2004) between MJD = 60076.47 and 60085.44 in *w2*, *m2*, *w1*, *u*, *b*, and *v*. The science-ready data were retrieved from the Swift archive.[21] In 2023 December, deep template images were obtained in all filters to remove the host contamination from the transient photometry. Then all sky exposures for a given epoch and filter were coadded to boost the signal-to-noise ratio using `uvotimsum` in HEAsoft[22] version 6.31.1. Afterwards, the brightness of the SN was measured with the Swift tool `uvotsource`. The source aperture had a radius of 5″, while the background region had a significantly larger radius. We measured the host contribution from the 2023 December templates using the same source and background apertures and subtracted this contribution from the transient flux measurements. All measurements were calibrated with the latest calibration files from 2021 November and converted to the AB system following Breeveld et al. (2011). Table 4 summarizes all measurements (not corrected for reddening).

2.5. Swift X-Ray Telescope Measurements

While monitoring SN 2023aew with UVOT between MJD = 60076.47 and 60085.44, Swift also observed the field with its onboard X-ray telescope (XRT) between 0.3 and 10 keV in photon-counting mode (Burrows et al. 2005). These data were analyzed with the online tools of the UK Swift team[23] that use the software package HEASoft version 6.32 and methods described in Evans et al. (2007, 2009).

SN 2023aew evaded detection in all epochs. The median 3σ count-rate limit of each observing block is 8×10^{-3} s^{-1} (0.3–10 keV). Coadding all data pushes the 3σ count-rate limits to 1.4×10^{-3} s^{-1}. A list of the limits from the stacking analysis is shown in Table 5. To convert the count-rate limits into a flux, a power-law spectrum was assumed with a photon index[24] of $\Gamma = 2$ and a Galactic neutral hydrogen column density of 3.4×10^{20} cm^{-2} (HI4PI Collaboration et al. 2016).

[21] https://www.swift.ac.uk/swift_portal
[22] https://heasarc.gsfc.nasa.gov/docs/software/heasoft/
[23] https://www.swift.ac.uk/user_objects/
[24] The photon index is defined as the power-law index of the photon flux density ($N(E) \propto E^{-\Gamma}$).

Table 1
Description of Spectrographs Used for Follow-up and the Corresponding Data Reduction Pipelines

Instrument	Telescope	Software
SEDM[a]	Palomar 60 inch	pySEDM[b]
ALFOSC[c]	Nordic Optical Telescope	PyNOT[d], PypeIt
DBSP[e]	Palomar 200 inch	DBSP_DRP[f]
KAST[g]	Shane 3 m	IRAF[h]
LRIS[i]	Keck I	LPipe[j]
SPRAT[k]	Liverpool Telescope	PypeIt
NIRES[l]	Keck II	Wilson et al. (2004)
ESI[m]	Keck II	makee[n]

Notes.
[a] Spectral Energy Distribution Machine (Blagorodnova et al. 2018).
[b] Rigault et al. (2019) and Kim et al. (2022).
[c] Andalucia Faint Object Spectrograph and Camera.
[d] https://github.com/jkrogager/PyNOT.
[e] Double Beam Spectrograph (Oke & Gunn 1982).
[f] pypeit (Prochaska et al. 2020) based pipeline (https://github.com/finagle29/dbsp_drp).
[g] Kast Double Spectrograph (Miller & Stone 1987).
[h] Tody (1986, 1993).
[i] Low Resolution Imaging Spectrometer (Oke et al. 1995).
[j] IDL-based automatic reduction pipeline (Perley 2019; https://sites.astro.caltech.edu/~dperley/programs/lpipe.html).
[k] Spectrograph for the Rapid Acquisition of Transients (Piascik et al. 2014).
[l] Near-infrared Echellette Spectrometer (Wilson et al. 2004).
[m] Echellette Spectrograph and Imager (Sheinis et al. 2002).
[n] https://www2.keck.hawaii.edu/inst/esi/makee.html.

The coadded count-rate limit corresponds to an unabsorbed flux of $<5.5 \times 10^{-14}$ erg cm^{-2} s^{-1} between 0.3 and 10 keV and a luminosity of $<7.8 \times 10^{40}$ erg s^{-1}. The flux and luminosity limits of the individual bins are shown in Table 5.

2.6. Optical Spectroscopy

We obtained a comprehensive spectroscopic follow-up data set from many facilities at a variety of spectral resolutions (e.g., Keck I/LRIS $R \sim 800$–1400, P200/DBSP $R \sim 1000$, NOT/ALFOSC $R \sim 360$, P60/SEDM $R \sim 100$) to study the evolution of this SN. In total, we have 41 spectra covering epochs from 34 to 281 days since explosion. Table 1 lists the facilities, instruments, and data processing software references. The spectral sequence is listed in Table 2 and shown in Figure 2. All the spectra were corrected for Milky Way extinction using the same procedure as for the photometry, then scaled to match the synthetic photometry from the spectra with the contemporaneous host-subtracted ZTF r-band data. The SN redshift ($z = 0.0255 \pm 0.0001$) was obtained from the narrowest lines in our highest-resolution Keck II/ESI spectrum in the absence of a preexisting host redshift measurement. The spectra will be made available on WISeREP[25] (Yaron & Gal-Yam 2012).

3. Analysis

3.1. Light Curve

SN 2023aew had a rise of about 2.5 mag over the first 25 days (∼11 mag/100 days) to a first peak in TESS data, with a peak magnitude of 17.88 mag in the TESS-Red band (−17.2; see Figure 1). It then proceeded to decline at an initial rate of 2.6 mag/100 days in the r band for the next 30 days (rest-frame) and settled onto a slowly declining plateau of only 0.2 mag/100 days in the r band between days 60 and 105, reaching a minimum brightness of 18.93 mag (−16.5). After day 105, SN 2023aew suddenly started brightening again and rose at a rate of 13.5 mag/100 days in the r band; it reached a second peak brightness of 16.45 mag (−18.8) at day 132, after which it started turning over to decline at a rate of ∼4 mag/100 days (r band). Around day ∼205, the SN developed a smaller bump in the light curve for ∼25 days, before coming back to its previous decline rate. Our last detection of 21.2 mag in the i band was obtained on day 315, and the last limit of >22.1 mag in the r band was obtained on day 323. Figure 1 also shows the light curves of some peculiar SESNe from the literature for comparison. The light curves of comparison SNe were obtained from the Open Supernova Catalog (Guillochon

[25] https://www.wiserep.org/

Table 2
Summary of Optical and Near-infrared Spectra

MJD	Phase (day)	Telescope/Instrument	Int. (s)
59972	34	P60/SEDM	2250
60044	105	LT/SPRAT	2200
60056	117	P60/SEDM	1800
60057	118	P60/SEDM	1800
60058	119	NOT/ALFOSC	1800
60058	119	P60/SEDM	1800
60058	119	Lick-3 m/KAST	1200
60062	123	P60/SEDM	1800
60063	124	Keck II/NIRES	520
60065	126	LT/SPRAT	2200
60071	132	P60/SEDM	1800
60073	134	NOT/ALFOSC	600
60075	136	P60/SEDM	1800
60081	141	P60/SEDM	1800
60085	146	Keck I/LRIS	300
60087	147	P60/SEDM	1800
60103	163	P60/SEDM	1800
60108	168	P60/SEDM	1800
60110	170	Keck I/LRIS	180
60110	170	Keck I/LRIS	1200
60116	176	P60/SEDM	1800
60116	176	P200/DBSP	600
60120	179	NOT/ALFOSC	1800
60120	180	P60/SEDM	1800
60123	183	P60/SEDM	2250
60124	183	P60/SEDM	1800
60126	185	P60/SEDM	1800
60130	189	P60/SEDM	1800
60138	197	P60/SEDM	1800
60143	202	Keck I/LRIS	300
60144	203	NOT/ALFOSC	2400
60146	205	P60/SEDM	2250
60147	206	P60/SEDM	2250
60148	207	Keck I/LRIS	600
60155	214	P60/SEDM	2250
60161	219	NOT/ALFOSC	2400
60168	226	P60/SEDM	2250
60175	233	NOT/ALFOSC	4400
60199	256	NOT/ALFOSC	1100
60206	263	Keck II/ESI	2700
60224	281	Keck I/LRIS	900

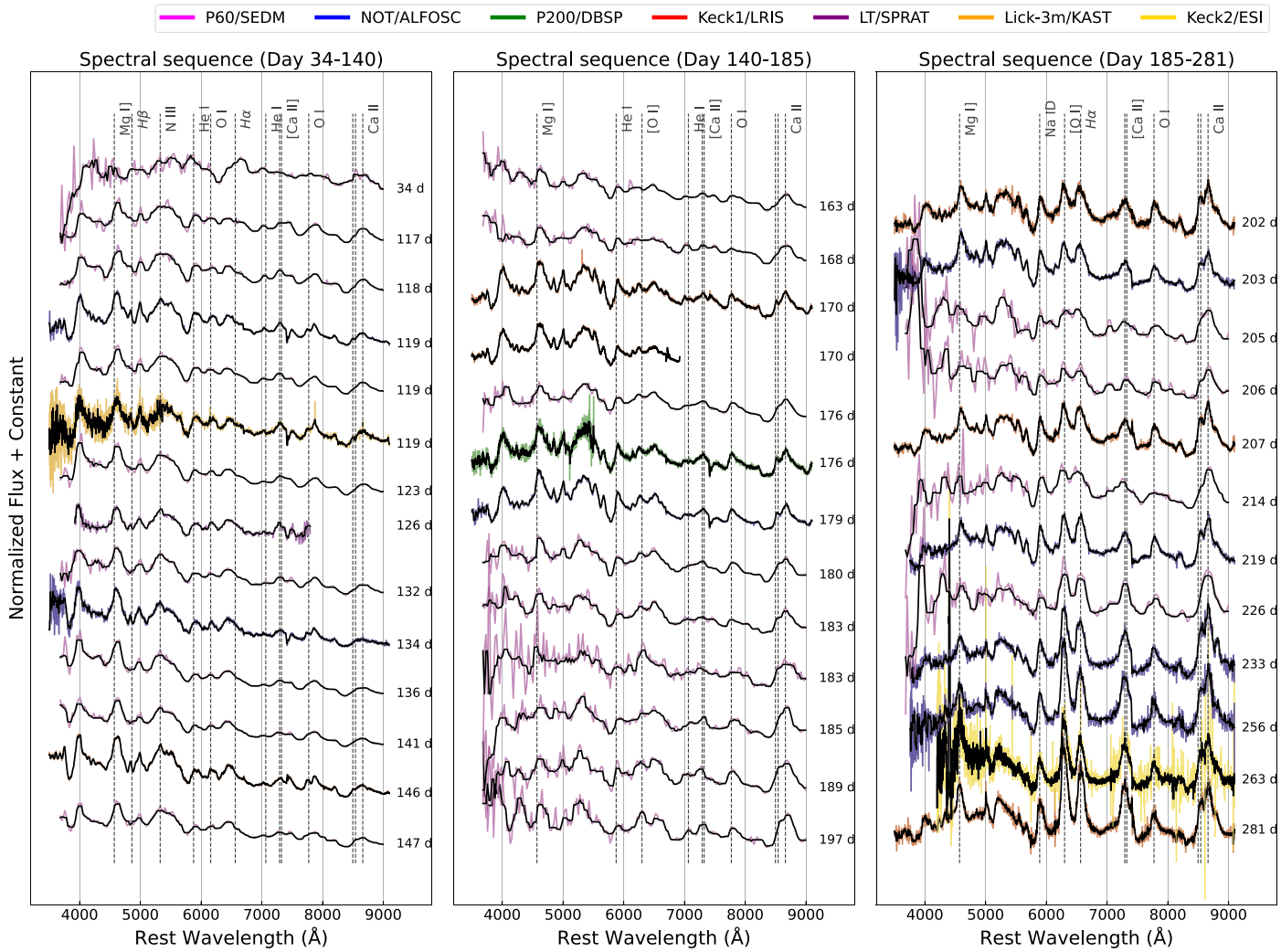

Figure 2. Spectral sequence of SN 2023aew from day 34 to day 281. The black lines are smoothened spectra (using the median filter) and the colored lines are original spectra, with different colors depicting different instruments. Some important spectral lines are marked with gray dashed lines. In the left panel, the Balmer lines are visible in the first spectrum at 34 days, then Hα seemingly shows up again in the nebular phase spectra in the third panel.

et al. 2017) for SNe 1993J (van Driel et al. 1993; Benson et al. 1994; Richmond et al. 1994, 1996; Barbon et al. 1995), 1998bw (Galama et al. 1998; Sollerman et al. 2000, 2002; Patat et al. 2001), 2005bf (Tominaga et al. 2005; Stritzinger et al. 2018), 2007gr (Valenti et al. 2008b; Bianco et al. 2014; Chen et al. 2014), 2009ip (Mauerhan et al. 2013; Margutti et al. 2014), 2011dh (Arcavi et al. 2011; Ergon et al. 2015), and iPTF13bvn (Fremling et al. 2016; Modjaz et al. 2016; Shivvers et al. 2019), and from ATLAS forced photometry service (Tonry et al. 2018; Smith et al. 2020; Shingles et al. 2021) for SN 2017ens (Chen et al. 2018).

Figure 3 depicts the $g-r$ and $r-i$ color evolution of SN 2023aew and the comparison SNe. During the declining phase of the first peak, the color of SN 2023aew is red and constant. During the rapid rebrightening the color gets rapidly bluer, then slowly turns red again, similar to the comparison SNe.

The UV colors obtained with Swift just after the second peak (see Figure 1) do not seem particularly bluer than those of other SESNe at those epochs. However, as there are only a few SESNe observed in UV, and they show a wide variety of behavior in their UV colors, no inferences can be made with certainty (Brown et al. 2009, 2015).

3.2. Bolometric Luminosity

SN 2023aew has good coverage in only the TESS-Red band for the first 30 days and then only in the *r* band for the rest of the duration of the first peak, after which there is decent coverage in all ZTF and ATLAS optical bands. However, as there is no coverage in the UV or the infrared, it is difficult to produce a full bolometric light curve.

The TESS-Red band fluxes were converted into luminosities by multiplying them with the effective filter width (integrated area under the transmission curve of the TESS-Red filter; Rodrigo et al. 2012; Rodrigo & Solano 2020) and the luminosity distance factor. This estimate was used as an approximate pseudo-bolometric luminosity.

We used `Superbol` (Nicholl 2018) with ZTF *gri* bands and ATLAS *co* bands to get pseudo-bolometric and bolometric light curves. `Superbol` interpolates all bands to the *r*-band epochs, calculates pseudo-bolometric luminosity by integrating the observed fluxes over the available bandpasses, and estimates the bolometric luminosity by adding blackbody corrections (absorbed UV, and near-infrared (NIR)) to the pseudo-bolometric light curve. Additionally, `HAFFET` (Yang & Sollerman 2023) was also used to obtain another bolometric

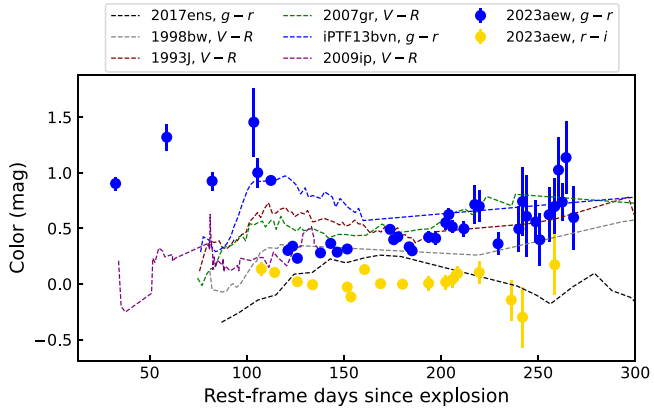

Figure 3. $g-r$ and $r-i$ color curves of SN 2023aew. Shown for comparison are $V-R$ color curves of SNe 1993J, 1998bw, 2007gr, and 2009ip, and $g-r$ color curves of SN 2017ens and iPTF13bvn.

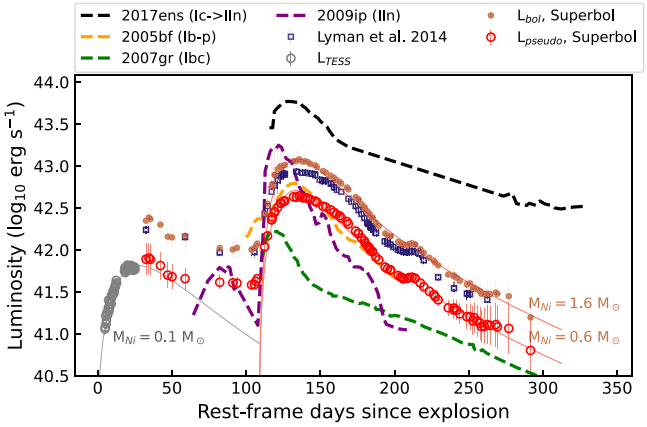

Figure 4. Bolometric (filled red circles) and pseudo-bolometric (open red circles) light curves of SN 2023aew along with some comparison SNe. Gray open circles denote the pseudo-bolometric luminosity approximation from TESS observations. Also shown (blue squares) is an alternative estimate of the bolometric light curve obtained by applying bolometric corrections to g-band data following Lyman et al. (2014). The fits of ^{56}Ni radioactivity power to the bolometric and pseudo-bolometric light curves following the Arnett method are plotted in light red for the second peak and gray for the first peak.

light-curve estimate by applying bolometric corrections to g-band data following Lyman et al. (2014).

Figure 4 shows both the bolometric luminosity and the pseudo-bolometric luminosity for SN 2023aew along with luminosities of SNe 1998bw (pseudo-bolometric light curve from Figure 18 of Patat et al. 2001), 2005bf (bolometric light curve from Figure 8 of Folatelli et al. 2006), 2007gr (pseudo-bolometric light curve from Figure 6 of Chen et al. 2014), 2009ip (bolometric light curve from Figure 11 of Margutti et al. 2014), and 2017ens (pseudo-bolometric light curve from Figure 1 of Chen et al. 2018). The pseudo-bolometric luminosity of the first peak reached a maximum of $(6.6\pm0.2)\times10^{41}$ erg s^{-1}, while the second peak reached a maximum of $(4.4\pm0.6)\times10^{42}$ erg s^{-1}. The maximum bolometric luminosity of the second peak is $(1.2\pm0.2)\times10^{43}$ erg s^{-1}.

The pseudo-bolometric light curve from TESS data was integrated to obtain the radiated energy output over its duration, and it came out to be $(8.0\pm0.6)\times10^{47}$ erg. The bolometric light curve was integrated for the rest of the first peak (until day 100) and came out to be $(8.8\pm0.4)\times10^{48}$ erg. Hence a lower limit of $(9.6\pm0.5)\times10^{48}$ erg can be placed on the total radiated energy during first peak. For the second peak (from rebrightening until our last photometry point at 294 days since explosion), the radiated energy is $(5.60\pm0.13)\times10^{49}$ erg. Thus the total energy radiated by SN 2023aew from explosion until our last detection is $(6.56\pm0.18)\times10^{49}$ erg. Comparison of this radiated energy with other similar events is further discussed in Section 4.2.

Assuming the two peaks are separate SESNe, we fit ^{56}Ni power luminosity models using the Arnett method (Arnett 1982; Valenti et al. 2008a) separately to both peaks. For the first peak, we use the pseudo-bolometric luminosity from TESS observations and from Superbol (see above) covering days 0 to 50 since explosion to fit the Arnett radioactivity model. We obtain lower limits on nickel mass, $M_{\rm Ni}=0.11^{+0.02}_{-0.06}\ M_\odot$, and ejecta mass, $M_{\rm ej}=27.6^{4.1}_{-19.0}\ M_\odot$, assuming a photospheric velocity of 11,800 km s^{-1} (see Section 3.3).

Next, assuming that the second brightening is also powered by ^{56}Ni decay, *gri* data during the rise of the second peak were fitted with power laws using `HAFFET` to obtain an "explosion" epoch, which came out to be ∼115 days after the explosion epoch from TESS. Using this explosion epoch as a reference, models were fitted to the bolometric and pseudo-bolometric light curves, which seem to agree well with the curves except around the bump at 210 days from explosion. The radioactivity power fit to $L_{\rm bol}$ requires a nickel mass, $M_{\rm Ni}=1.59^{+0.62}_{-0.40}\ M_\odot$, and an ejecta mass, $M_{\rm ej}=8.52\pm2.40\ M_\odot$, assuming a photospheric velocity of 6000 km s^{-1} (see Figure 11). A fit to the pseudo-bolometric luminosity provides lower limits of $M_{\rm Ni}=0.59^{+0.31}_{-0.19}\ M_\odot$ and $M_{\rm ej}=7.62\pm3.16\ M_\odot$. Clearly, this estimate of nickel mass is unreasonably high compared to what is observed in other SESNe and what is predicted from models, and thus must be hinting at an additional power source for the second peak.

Also, the radioactivity models for the "two SESNe" combined cannot explain the luminosity of the plateau that bridges the two peaks (see Figure 4), thus making the scenario of two separate SESNe less likely.

3.3. First Peak of SN 2023aew

Serendipitous coverage from TESS revealed the explosion epoch, the rise, and the peak of the first bump, which were not detected in any other data. The overall light-curve shape of SN 2023aew resembles that of SN 2009ip but is much broader in both peaks (see Figure 1). Figure 1 also compares the first peak with Type IIb SNe 1993J and 2011dh, which have a faster decline than SN 2023aew and narrower light curves. The rise time of the first peak from explosion epoch to peak is 20 rest-frame days, and from half-peak flux to peak flux is ∼9 rest-frame days. The decline time from peak to half-peak is ∼27 rest-frame days but is likely affected by the plateau that the first peak develops at 50 days. The half-peak to peak rise and decline times of the first peak are compared with those of a sample of bright supernovae obtained from the ZTF Sample Explorer[26] (Fremling et al. 2020; Perley et al. 2020; classified since the start of ZTF and having prepeak and postpeak coverage) in Figure 5. The rise of the first peak seems consistent with the BTS sample SNe, but the decline time is slightly longer than for the SESN sample and more toward those of the SN II population.

[26] https://sites.astro.caltech.edu/ztf/bts/explorer.php

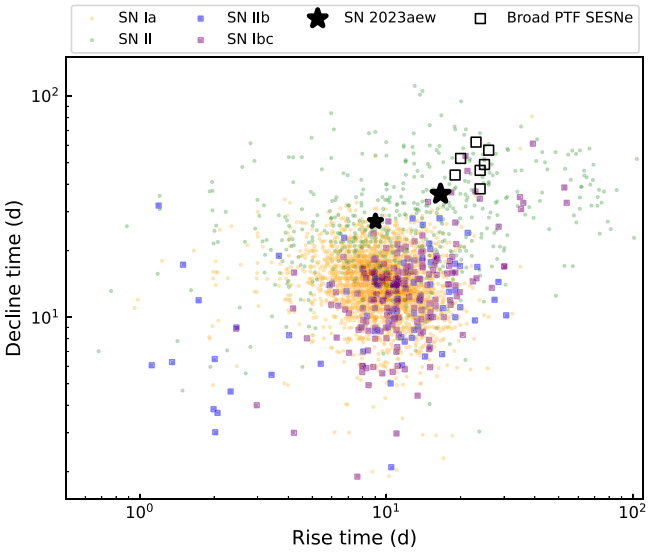

Figure 5. Rise time vs. decline time (peak to half-peak in the *r* band) of the Bright Transient Survey sample of supernovae (colored points) and broad light-curve SESNe from Karamehmetoglu et al. (2023; empty black squares). The first peak of SN 2023aew is marked with the smaller black star (rise time from TESS data) and the second peak is marked with the larger black star (*r*-band data).

After ZTF discovery, an initial spectrum at the first peak was obtained through the usual spectroscopic efforts of the BTS, which showed a P-Cygni Hα profile of with a velocity of $\sim$11,800 km s^{-1}. Using the Python version of template-matching supernova classification software `Superfit` (Howell et al. 2005; Goldwasser et al. 2022), a match to the Type IIb SN 2001ig was obtained and SN 2023aew was classified as an SN IIb (Section 1). Figure 6(a) shows that this earliest spectrum of SN 2023aew (+34 days from explosion) is a good match with the early-time spectra of Type IIb SNe 1993J (+28 days) and 2011dh (+5 days). The broad component of Hα is similar in velocity to the broad component of the precursor spectra of Type IIn SN 2009ip; however, any narrow components, if present, cannot be discerned in our SEDM spectrum. The deviation from 2009ip-like behavior occurs during the second peak, where SN 2023aew transforms into an SN Ibc and does not show any narrow lines in its spectrum.

3.4. Second Peak of SN 2023aew

For the second peak resulting from the rapid rebrightening, the rise time from half of the peak luminosity to peak luminosity is $\sim$17.5 rest-frame days, and the decline time from the peak to half of the peak luminosity is $\sim$36.1 rest-frame days. The light-curve width at half-maximum is $\sim$53.5 rest-frame days. These values are higher than what has typically been observed for normal SESNe (Prentice et al. 2016; Taddia et al. 2018). In Figure 5, the half-peak to peak rise and decline times of the second peak of SN 2023aew are compared with those of the BTS sample and the sample of broad light-curve SESNe from the Palomar Transient Factory presented in Karamehmetoglu et al. (2023). The second peak of SN 2023aew is indeed broader than what is the case for most ZTF SESNe and consistent with those in the broad Karamehmetoglu et al. (2023) sample. Though none of the SESNe in Karamehmetoglu et al. (2023) had as long a precursor-like first peak as SN 2023aew, some of them do display similar undulations in the light curve. Karamehmetoglu et al. (2023) favor ejecta from massive stars (>20–25 $M_{\odot}$) as the cause behind the broad light curves but do not rule out hidden interaction with the circumstellar medium (CSM) or additional powering mechanisms.

Figure 6(b) compares spectra taken around the second peak maximum of SN 2023aew to the mean spectra of SNe IIb, SNe Ib, and SNe Ic at peak (0 ± 2 days) as constructed in Liu et al. (2016). The absorption feature at He I λ5876 appears to be closer in strength to an SN Ib rather than an SN Ic, with perhaps a weak helium feature present also at 7065 Å. On the other hand, with He I $\lambda\lambda$6678, 7065 being weak or absent, the 5876 Å feature could be due to Na I D instead, making a stronger case for a spectral similarity to SNe Ic. The presence of trace helium in SNe Ic is also highly debated (Branch et al. 2002; Elmhamdi et al. 2006); however, Liu et al. (2016) suggest that for a true SN Ib classification either the 5876 Å line should be strongly identified before maximum or all three He I lines (5876, 6678, 7065 Å) should be present post-maximum and at <40 days. Considering the phase of SN 2023aew to be near maximum (and second brightening to be the main peak) and given that the 5876 Å line is clearly present, we suggest that SN 2023aew resembles more an SN Ib at this phase. There is an absorption line around $\sim$6200 Å that matches the Hα absorption from the earliest spectrum; however, the corresponding emission peak is blueshifted from the Hα rest wavelength and redshifted from Si II λ6355. Several studies (Matheson et al. 2001; Branch et al. 2002; Elmhamdi et al. 2006; Yoon et al. 2010; Liu et al. 2016; Parrent et al. 2016) have indicated the presence of trace hydrogen in SNe Ib and that the origin of similar features around 6000–6400 Å in SNe Ib could be blueshifted emission of Hα (Section 3.1 of Gal-Yam 2017).

Figure 6(c) compares post-second-peak decline spectra of SN 2023aew with SESN mean spectra of Liu et al. (2016) at 20 ± 2 days past maximum. The spectral evolution of SN 2023aew is slow, but at this stage it has started developing [O I] λ6300 and strong Ca II NIR emission. Absorption near He I λ5876 is strong, but likely Na I D at this stage and the other He I lines are much weaker compared to the SN Ib mean spectrum. The overall spectra at this stage appear more similar to the SN Ic than to the SN Ib template, which is also supported by SNID matches to SN Ic templates (Hoogendam et al. 2023).

An NIR spectrum was also obtained with Keck II/NIRES covering the wavelength range from 1.0 to 2.4 μm but unfortunately the data have poor signal-to-noise ratio. Figure 7 shows the NIR spectrum along with some possible line identifications. The Paschen series is marked, as well as He I around 1.085 μm. Paα falls in a no-coverage zone, and Paβ and Paδ fall in high-noise regions, hence are not clearly discernible in the spectrum. The feature near 1.1 μm could be either Paγ or He I, but the helium line at 2.2 μm is not detected.

3.5. Nebular Spectra and Emergence of Hα

Figure 6(d) compares spectra taken around the late-time bump at $\sim$200 days from explosion to nebular spectra of SESNe 1993J (IIb; Barbon et al. 1995; Matheson et al. 2000), 2011dh (IIb; Yaron & Gal-Yam 2012; Ergon et al. 2015), 2005bf (Ib-pec; Shivvers et al. 2019), and 2007gr (Ic; Shivvers et al. 2019) obtained from the Open SN catalog. The strongest features present at this stage are Ca II NIR, [Ca II] $\lambda\lambda$7292, 7324, O I λ7774, [O I] $\lambda\lambda$6300, 6364, Na I D λ5890, and an

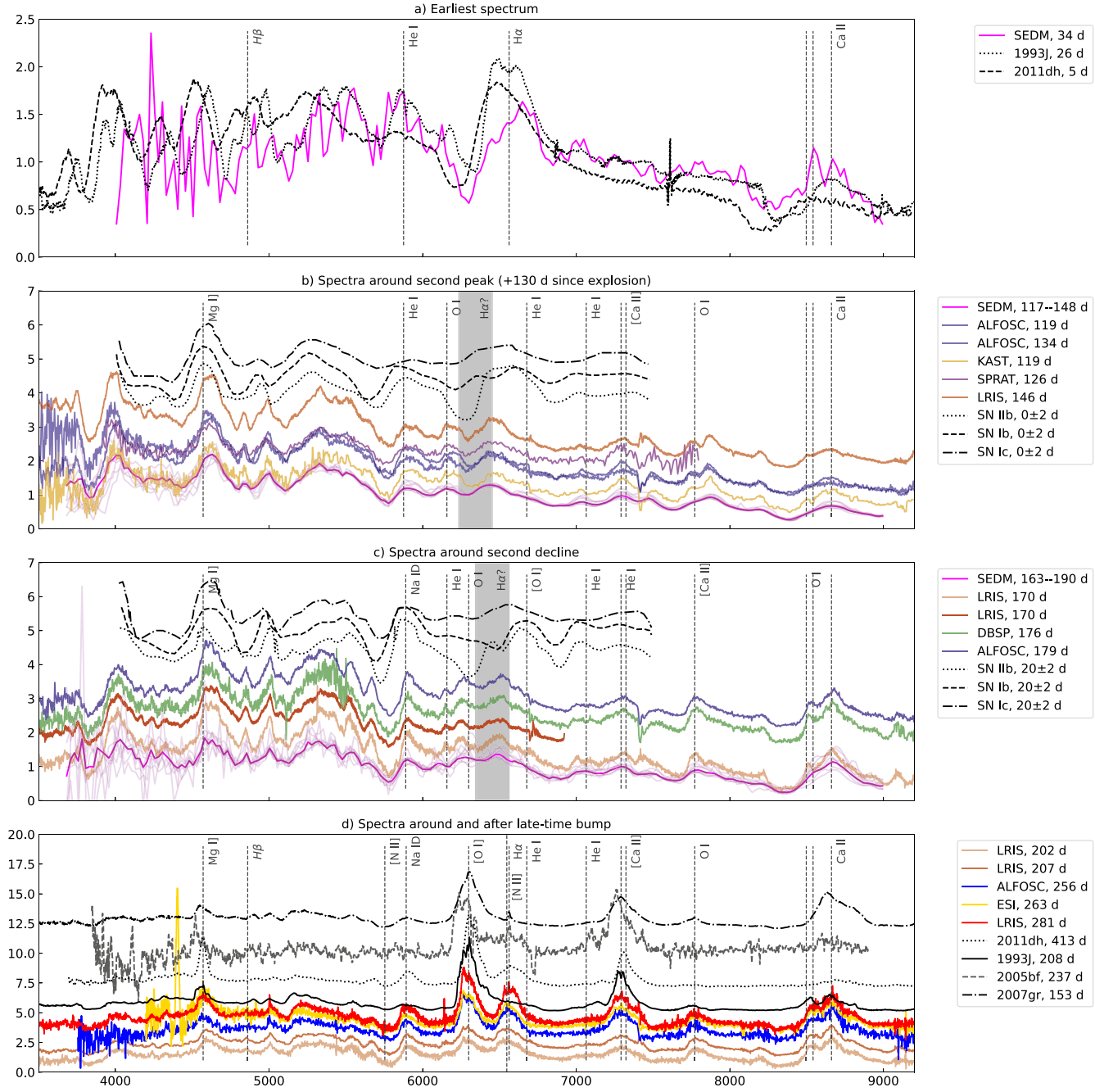

Figure 6. SN 2023aew spectral comparison at different phases compared to mean spectra of SNe IIb, SNe Ib, and SNe Ic from Liu et al. (2016).

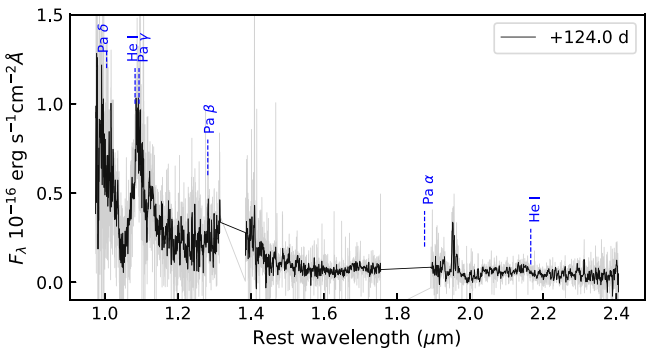

Figure 7. A near-infrared spectrum of SN 2023aew obtained with Keck II/NIRES, smoothened using a median filter with a kernel size of 9 pixels (in black). Tentative line identifications are marked with blue dashed lines.

emission feature centered around Hα. [N II] $\lambda\lambda$6548, 6583 is also a major contributor of flux around the Hα wavelength at the nebular phases at the low-mass end of SESNe (low-mass Type IIb, Jerkstrand et al. 2015), but almost absent for the high-mass SESNe. The same is reflected in the spectra of comparison SESNe in Figure 6(d), with SN 2011dh (IIb) having the most flux in the [N II] line and SN 2007gr (Ic) barely having any. However, SN 2023aew seems to have a larger flux in that line than the others, possibly due to a contribution from Hα. Hβ is almost nonexistent, but is also similarly weak in the day 208 spectrum of SN 1993J.

To further explore the nature of SN 2023aew, flux ratios of nebular diagnostic lines are compared with the analysis of SESNe presented in Fang et al. (2019, 2022). The line fluxes of [O I] $\lambda\lambda$6300, 6364, [Ca II] $\lambda\lambda$7292, 7324, and [N II]/Hα

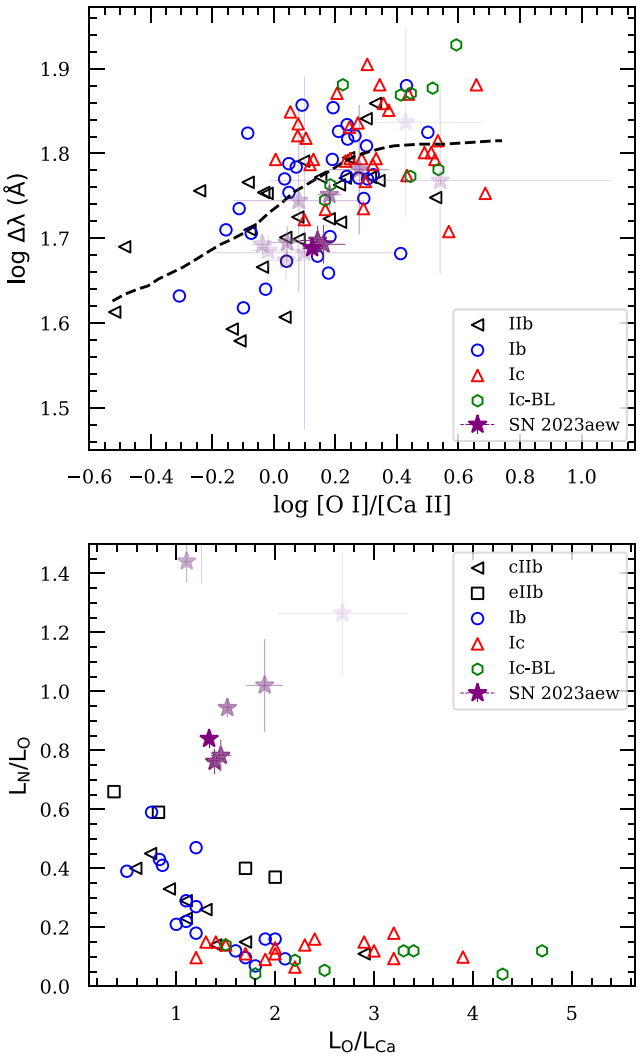

Figure 8. Top panel: SN 2023aew in the logarithmic phase space of [O I] width vs. [O I]/[Ca II] flux ratio for SESNe published in Fang et al. (2022, their Figure 7(a)). Bottom panel: L_N/L_O vs. L_O/L_{Ca} for SESNe published in Fang et al. (2019, their Figure 3). "cIIb" and "eIIb" refer to compact and extended SNe IIb respectively. Values for SN 2023aew are shown as purple stars and derived from late-time spectra (phases ranging from 200 to 281 days from explosion) with the transparency decreasing with increasing phase. The SN nebular spectra used in Fang et al. (2019) range from 150 to 300 days after the peak, while for SN 2023aew they range from 75 to 150 days after the second peak. SN 2023aew consistently shows higher values on the [N II]/[O I] axis, which suggest the presence of Hα contaminating (or rather dominating) the [N II] lines at these phases.

complex, and the width of the [O I] line, are calculated for SN 2023aew following similar procedures to those in Fang et al. (2019, 2022). The top panel of Figure 8 plots the correlation of the [O I]/[Ca II] ratio versus the [O I] width for SN 2023aew along with data obtained from Figure 7(a) of Fang et al. (2022). The bottom panel of Figure 8 plots the line ratio of [N II]/[O I] versus the line ratio of [O I]/[Ca II] for SN 2023aew along with data obtained from Figure 3 of Fang et al. (2019). The [O I] fluxes were calculated by fitting and subtracting a pseudo-continuum from the oxygen–nitrogen complex, then fitting and subtracting a Gaussian profile centered at 6563 Å to remove the [N II]/Hα contribution, and finally integrating the remaining flux in the complex over a suitable wavelength range. The [N II] fluxes were similarly calculated by subtracting a Gaussian profile fit centered at 6300 Å to remove the [O I] contribution after continuum removal. The [Ca II] fluxes were calculated after subtracting a pseudo-continuum and integrating over the line. The uncertainties were calculated using the Monte Carlo method as described in Appendix A. In both panels, the measurements for SN 2023aew are marked with purple stars having decreasing transparency with increasing phase.

Fang et al. (2022) discerned that oxygen-rich ejecta expand faster and the SESN subtype distribution showed that SNe IIb/Ib are more steeply correlated than SNe Ic/Ic-BL (see their Figure 7(a) and top panel of our Figure 8). SN 2023aew has $\log_{10}([\text{O I}]/[\text{Ca II}]) \sim 0.1$, before the correlation curve in Figure 8 (top panel) starts to flatten, but has lower velocities, again more toward the phase space that SNe IIb/Ib occupy. The luminosity ratio of [N II]/[O I] in Figure 8 (bottom panel) is considerably higher than the corresponding values Fang et al. (2019) measured for SESNe at that L_O/L_{Ca}, once again suggesting the presence of hydrogen in the nebular phase.

Further arguments for the 6500 Å feature consisting mostly of hydrogen are found when comparing to Barmentloo et al. (2024). In this work, the authors compare [N II] emission from a set of nebular model spectra to a sample of observed SESNe. They find that up until ∼200–250 days post-explosion, the contribution of [N II] in this region is below 50% for all progenitor models, with the feature being almost nonexistent for $M_{\text{preSN}} \gtrsim 4.5\ M_\odot$. Perhaps more importantly, it is found that the line widths for the [N II] feature in their sample have a lower-limit FWHM of 170 Å, with the median around ∼200–220 Å. Performing the same analysis for SN 2023aew, we find FWHM values between 115 and 135 Å. This means that if the feature were mostly [N II], SN 2023aew would be a significant outlier (as when comparing with Fang et al. 2022). Finally, calculating the $f_{[\text{NII}]}$ diagnostic from Barmentloo et al. (2024) for our spectral series, the resulting values would indicate $M_{\text{preSN}} \lesssim 3\ M_\odot$, which does not match with any of our earlier estimates. All in all, the above findings suggest that any presence of [N II] could only be very minor, with the majority of the emission in this region due to other elements, most probably hydrogen.

A final inference that can be derived from the nebular spectra comes from the line profiles of [O I] $\lambda\lambda$6300, 6364, [Ca II] $\lambda\lambda$7292, 7324, and Mg I] λ4571. Figure 9 shows the nebular line profiles with dashed vertical lines marking the rest line wavelengths and dotted vertical lines marking blueshifted (by 1500 km s^{-1}) wavelengths. The [O I] profile clearly has blueshifted components for both the 6300 and 6364 Å lines, creating a double-peaked profile. [Ca II] also has hints of double-peaked structure with peaks blueshifted by 1500 km s^{-1}, though not as clearly as for [O I]. The Mg I] peak is redshifted at earlier epochs but a blueshifted component seems to develop at later times. The blueshifted peak in all three lines seems to get stronger with time. The double-peaked shape can also be discerned in O I λ7774 and in the Hα/[N II] complex for some epochs. Double-peaked structure in [O I] lines has been observed in nebular spectra of many SESNe (Modjaz et al. 2006, 2008; Maeda et al. 2007; Modjaz 2007), and in most cases, the two peaks are symmetric around the rest wavelength (for example, see Figure 2 of Modjaz et al. 2008). SN 2005bf (Folatelli et al. 2006; Maeda et al. 2007), a peculiar Type Ib SN, was an exception with a highly blueshifted (∼2000 km s^{-1}) trough, similar to what is seen here for

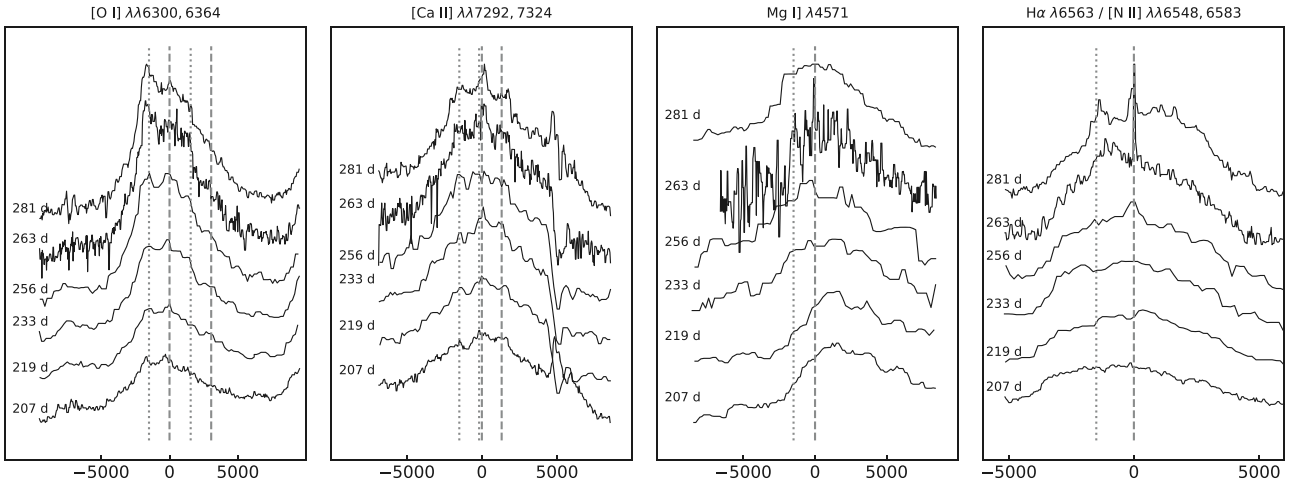

Figure 9. Line profiles of nebular [O I], [Ca II], Mg I], and Hα/[N II] complex from 207 to 281 days. Dashed vertical lines mark the rest wavelengths and dotted vertical lines mark the blueshifted ($\sim$1500 km s^{-1}) components. The blueshifted component in all lines appears to be increasing in strength with phase.

SN 2023aew. An aspherical explosion in the shape of a torus could give rise to a double-peaked feature in the case of optically thin ejecta at nebular times but does not explain the blueshift. For SN 2005bf, a unipolar blob of low mass, accelerated by a pulsar kick, was suggested by Maeda et al. (2007). On the other hand, less extreme blueshifts can be explained by residual opacity effects as described in Taubenberger et al. (2009). More recently, Fang et al. (2024) analyzed a sample of nebular spectra of SESNe and found that roughly half of the SESNe had either a double-peaked [O I] or [Ca II] but none had double-peaked structure in both lines. Fang et al. (2024) theorize an axisymmetric model for their observations, where the oxygen-burning ash (Ca-rich region) is distributed in bipolar bubbles with unburnt oxygen outside it, and depending on the viewing angle this leads to a double-peaked profile in one of the lines. However, applying this prescription to SN 2023aew is difficult due to the structure present in the calcium line and the blueshifted trough. More advanced 3D models are just beginning to be explored (e.g., van Baal et al. 2023).

4. Discussion

4.1. Two Distinct Supernovae or a Single Peculiar One?

To determine whether the light curve of SN 2023aew is due to a single transient or potentially due to two separate events, such as two SNe that just happened to explode very close in time and space (along the line of sight), we imaged SN 2023aew with WaSP (Wafer-Scale Imager for Prime) on the Palomar 200 inch telescope (P200) in g, r, and i bands 144 days after explosion, right around the second peak. The exposure time used per band was 300 s, which corresponds to a 5σ limiting magnitude of $\sim$22.5 mag for WaSP in good seeing conditions. The SN was observed at an average seeing of 1.″4. On the same night, a confirmed sibling SN Ia pair, SN 2023egs, with peaks separated by $\sim$20 days and on-sky separation of $\sim$1.″6 was also observed with WaSP. The first SN Ia of this pair was $\sim$50 days past maximum at the time of observation and thus would be at least 3 mag fainter than peak (18.4 mag) if it was a normal SN Ia (Phillips & Burns 2017), making it $\gtrsim$21 mag. The second SN was $\sim$19 mag at the time of observation and both SNe Ia in SN 2023egs were clearly detected in the WaSP image. Considering the initial decline of the first peak of SN 2023aew (2.6 mag/100 days), the "first" SN in SN 2023aew at 144 days from explosion would be $\sim$21.1 mag, while the second SN was $\sim$16.7 mag, and thus both would still be separately detected in WaSP data if they were $\sim$2″ apart. Upon analyzing the WaSP observations of SN 2023aew, there did not seem to be two sources present at the location of SN 2023aew within the seeing limit.

Graham et al. (2022) analyzed sibling SNe (SNe sharing the same host galaxy) in the ZTF BTS sample of two years and found five sibling pairs (10 SNe) brighter than 18.5 mag, corresponding to a rate of only $\sim$1% of total SNe in BTS in that same period. Out of these, only two were SESNe, i.e., about one per year. The lowest on-sky separation of these siblings was 3.″7. Thus, the chances of SN 2023aew being an SESN sibling pair with coincident location (<2″) and also exploding within $\sim$115 days (4 months) of each other is extremely small.

Post-facto statistics is difficult, but another crude estimate of the rarity of SN 2023aew being a sibling pair might be calculated as follows. Assuming an SN rate of 1 per 100 yr per galaxy, the Poisson probability of two SNe exploding within half a year is $P_1 \sim 1 \times 10^{-5}$. As SN 2023aew is roughly 7 kpc from the center of its host, the probability of the siblings occurring at that radius also needs to be taken into account. This probability can be estimated by taking the radial distribution of CCSNe in a galaxy from Figure 2 of Wang et al. (1997), then calculating the ratio of the integrated distribution over a radius span of 6–8 kpc to the integrated distribution over the galaxy span (assuming $\sim$20 kpc), which comes out to be $P_2 \sim 0.14$. From the P200/WaSP image, the on-sky separation is known to be within 2″, which translates to $\sim$1 kpc at the distance of SN 2023aew. Thus the fraction of volume of the 6–8 kpc disk that the siblings are expected in would be at most $P_3 \sim 0.01$. The exact off-center distance to the host is of course not important, but the fact that the SN exploded in the outskirts of a resolved galaxy where the star formation rate is limited makes the probability of two unrelated SNe much smaller. Thus the total probability of two SESNe exploding within 0.5 yr in the same galaxy at $\sim$7 kpc from the galaxy center and within 2″ on-sky separation is $P \sim 1.7 \times 10^{-8}$ per galaxy. Next, the maximum distance out to which SN 2023aew ($M_{\rm abs}^{\rm peak} \sim -18.7$) would be detected and classified by the BTS survey (flux limit of 18.5 mag) is $\sim$275 Mpc. Taking the density of galaxies in this volume

(assuming MW-like) to be $\sim$0.006 Mpc^{-3}, assuming a uniform distribution, and accounting for the fact that ZTF can only observe $\sim$0.75 of the sky, the number of galaxies ZTF will observe in a volume of 275 Mpc is $\sim$392,000. Multiplying that with the probability per galaxy, the expected number of siblings like SN 2023aew is $\sim$0.007, and hence the Poisson probability of detecting one event is 0.7%. Even more unlikely is the probability that both of these events are SESNe; in particular, the unusual properties of the second peak in terms of lower-than-average line velocities and a broader-than-average and more luminous peak make it very unlikely that the events are not linked. We also do not know of any mechanism that would make one SN trigger the other in a common system on such short timescales.

4.2. Rebrightening or Precursor?

The usual interpretation for supernova rebrightening is that it is caused by interaction with a CSM shell ejected during the final moments of the progenitor. This is most frequently observed in SNe IIn, where the light curves have multiple undulations and late-time emission; see, for example, Nyholm et al. (2017). SN 2021qqp (Hiramatsu et al. 2024) had a long, slow-rising precursor before the first peak as well as a late-time brightening after about a year, with both first and second peaks showing spectral similarity. Late-time emission due to CSM interaction has also been observed in spectrally normal SESNe that develop narrow emission lines and secondary light-curve plateaus or peaks, some examples being SNe 2017ens (Chen et al. 2018) and 2019oys (Sollerman et al. 2020). In the case of SN 2023aew, the second peak is spectrally different (Ibc-like) from the first (IIb-like), unlike SN 2021qqp, and even though the SN light curve shows undulations, it does not evolve into having interaction-dominated spectra with narrow lines like SNe 2017ens and 2019oys. Hydrogen is present during the first peak but not during the second one and then comes back again in the nebular phase, but it has broader velocities than strongly interacting SNe IIn. If CSM interaction is indeed the cause of the rebrightening, the corresponding spectral signs are hidden. The horned and blueshifted [O I] and [Ca II] emission line profiles (see Figure 9), which could arise due to asymmetric gas distribution (SN 2005bf; Tominaga et al. 2005; Maeda et al. 2007; Modjaz et al. 2008), also hint at unusual geometry that could possibly hide the spectral signatures of interaction. Sollerman et al. (2020) presented two interacting SESNe, one where the dramatic light-curve transformation was accompanied by spectral interaction signatures while the second only depicted slight undulations. Hence it is less likely for such a dramatic rebrightening to not be associated with transformation into an interacting SN.

Other suggested causes of double peaks include double-peaked nickel distribution in the ejecta (SN 2005bf; Tominaga et al. 2005) and delayed magnetar energy injection (Maeda et al. 2007). However, the timescales from both of these scenarios are not consistent with the evolution of SN 2023aew (Kasen et al. 2016; Orellana & Bersten 2022).

Another possibility is the first peak being a precursor emission (Ofek et al. 2014; Strotjohann et al. 2021) similar to SN 2009ip (Mauerhan et al. 2013; Pastorello et al. 2013; Margutti et al. 2014). Precursors have also been seen in hydrogen-deficient SNe (Brennan et al. 2024). The upper panel of Figure 10 compares the light curves of SN 2023aew (circles) and SN 2009ip (dashed lines) and many similarities are

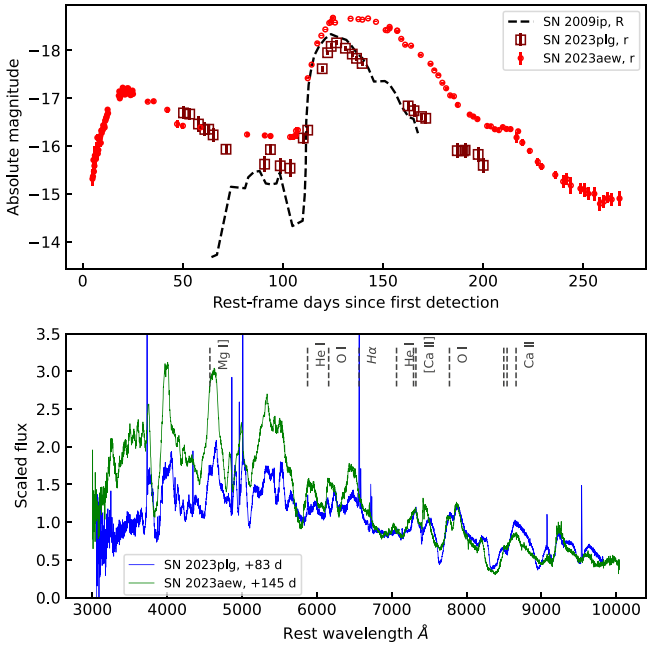

Figure 10. Comparison of SN 2023aew with the canonical precursor Type IIn SN 2009ip, but also with the analogous SESN SN 2023plg, showing both a similar luminous, long-lived declining precursor and a bright second peak. Light curves are shifted to match the rise of the main peak. SN 2023plg also exhibits a Type Ibc SN spectrum.

apparent. While SN 2023aew has a more luminous and longer precursor than SN 2009ip, the subsequent main peak is also more luminous and broader, and both SNe show undulations in their declining light curves. The rise time of the main peak is also similar in both SNe. However, the SN 2023aew precursor is much redder than the SN 2009ip precursor (see Figure 3). SN 2009ip also showed clear narrow, intermediate, and broad velocity features in the Hα emission line, and thus it was evident that circumstellar material was present and interacting with the SN ejecta; it was a clear Type IIn SN. However, for SN 2023aew, given that the only spectrum taken during the precursor event is from P60/SEDM, only the broad velocity feature can be resolved (11,800 km s^{-1}), which is similar to the broad velocity feature seen in SN 2009ip.

Let us assume for a moment that SN 2023aew is similar to a 2009ip-like event, with the first peak being due to an eruption (a precursor) and the second peak the actual supernova explosion. The longer and much more energetic precursor outburst could be generating energy when the SN ejecta later run into this material to power the second peak in addition to radioactive ^{56}Ni. An eruption mechanism could be considered for the precursor following the models in Matsumoto & Metzger (2022), wherein the precursor light curve is recombination-driven similar to Type IIP SNe. Though not observed in the first peak of SN 2023aew, perhaps due to inadequate spectral resolution, we assume a similar narrow line velocity as for SN 2009ip ($\sim$1500 km s^{-1}) in the following calculations.

Matsumoto & Metzger (2022) found that their semianalytical models largely follow the Popov (1993) analytical scalings (Equations (19) and (20) of Matsumoto & Metzger 2022). For SN 2023aew, the plateau duration ($t_{\rm pl}$) of the "precursor" is 80 days (which is a lower limit considering possible interruption by the subsequent SN explosion), and its radiated energy is $E_{\rm pl} \approx 1.0 \times 10^{49}$ erg, which gives a plateau luminosity for the

precursor ($L_{\rm pl} = E_{\rm pl}/t_{\rm pl}$) of 1.5×10^{42} erg s^{-1}. Then using the inverted Popov equations and an ejecta speed of $v_{\rm ej} \approx 1500$ km s^{-1}, we estimate an ejecta mass of $M_{\rm ej} \approx 0.61\ M_{\odot}$ and an initial radius of $R_0 \approx 9774\ R_{\odot}$ for the precursor; both values are comparable to those of the SNe analyzed in Matsumoto & Metzger (2022). Then again from Matsumoto & Metzger (2022, Equations (27) and (28)), we obtain an outer radius of the precursor ejecta $R_{\rm CSM} \sim 1 \times 10^{15}$ cm and a density of the precursor ejecta $\rho_{\rm CSM} \sim 2.6 \times 10^{-13}$ g cm^{-3}, which is a more extended and less dense CSM than for SN 2009ip (see Figure 8 of Matsumoto & Metzger 2022). Such a CSM, coupled with asymmetric geometry (signatures of which are present in the form of double-peaked nebular lines) could potentially result in an SN–CSM interaction without narrow lines in the optical spectra. Estimating the luminosity from shock heating using Equation (29) of Matsumoto & Metzger (2022), we get $L_{\rm sh} \approx 2 \times 10^{43}$ erg s^{-1}, assuming a radiative efficiency of 0.1 and $v_{\rm SN} = 6000$ km s^{-1}, which broadly agrees with the observed main peak luminosity. We discuss the possible mechanisms that can cause such eruptive mass loss as well as other possible progenitor scenarios in Section 4.3.

Interestingly enough, there is a recent analog of SN 2023aew, in terms of the precursor-like ZTF light curve (there are no TESS data to constrain the explosion in this case). SN 2023plg was discovered by ZTF and reported to TNS by ALeRCE on 2023 August 14 with a reported apparent magnitude of 18.7. The ZTF light curve of SN 2023plg tracks closely that of SN 2023aew, both being very red during the initial decline then brightening suddenly and maintaining a broad second peak. During the second peak, SN 2023plg was classified as an SN Ib on TNS by ePESSTO, but no spectroscopic data are available for the first peak. Close examination of more spectra suggests weak He I lines similar to what we see in SN 2023aew. The comparison is shown in Figure 10, with light curves in the upper panel and Keck I/LRIS spectra of both SNe in the lower panel. SN 2023plg is being followed up for future studies.

4.3. Origin of SN 2023aew

In this section, we discuss several scenarios that might explain the peculiar nature of SN 2023aew. We list several possibilities but leave a more detailed assessment and modeling of each scenario for a future study.

The precursor activities observed in SNe are often associated with mass ejection from their progenitors shortly before their explosions. One possible scenario to explain SN 2023aew is a mass ejection forming the precursor (first peak) followed by an SN explosion that shapes the major (second) light-curve peak. In the case of SN 2023aew, a hydrogen feature was observed during the precursor, which weakens during the subsequent brighter phase. Thus, the pre-SN mass ejection may have resulted in the ejection of all the remaining hydrogen-rich envelope in the progenitor, and the subsequent SN became a hydrogen-poor stripped-envelope SN. Thus, the progenitor might have been similar to those of Type IIb SNe and retained a small amount of hydrogen-rich envelope. Several stripped-envelope SNe are known to have a nearby hydrogen-rich CSM (e.g., SN 2014C, Milisavljevic et al. 2015; SN 2017ens, Chen et al. 2018). SN 2023aew could be an extreme case of a similar kind where the final ejection of the hydrogen-rich envelope occurred immediately before the explosion forming the precursor, and the subsequent SN is observed as hydrogen-poor.

There are several suggested mechanisms that can trigger the mass ejection shortly before the explosions of massive stars. For example, explosive nuclear shell burning may occur in the final stages of the evolution of massive stars, triggering a strong mass ejection (e.g., Woosley & Heger 2015). Mass ejection may also be triggered by an acoustic wave initiated by the strong convective motion in the core of massive stars shortly before explosion (e.g., Quataert & Shiode 2012; Fuller & Ro 2018). However, in both cases, the predicted energy that can be released is lower than the precursor energy estimated in SN 2023aew (see, e.g., Leung et al. 2021; Wu & Fuller 2021; Matsumoto & Metzger 2022). If the progenitor is in a close binary system with a compact companion, the accretion to the companion may help in providing additional energy to form the bright precursor (Tsuna et al. 2024).

Close passage of a massive star in an eccentric binary system could also result in precursor outbursts and was suggested for η Car (Damineli et al. 1997) by Soker (2001, 2004), Kashi & Soker (2010), and Smith (2011). Soker & Kashi (2013) explored a merger–burst model (non-terminal) for SN 2009ip where the precursor outbursts were explained by close periastron passages of the massive stars, and nonspherical CSM (torus-like) is naturally expected from these encounters.

Another possibility is a pulsational pair-instability SN (Woosley et al. 2007). Pulsational instability SNe are transients caused by a partial mass ejection of very massive stars triggered by the pair instability. A pulsational mass loss forming the precursor phase can occur several months before the final collapse of the massive stars. The final collapse may result in an SN explosion forming the major light-curve peak as observed in SN 2023aew. For example, some pulsational pair-instability SN models presented in Woosley (2017) have a similar luminosity to the precursor of SN 2023aew. It is possible that the progenitor of SN 2023aew experienced pulsational pair-instability mass ejection followed by an SN explosion. Although the progenitors of pulsational pair-instability SNe are expected to be massive ($\gtrsim 30\ M_{\odot}$, e.g., Renzo et al. 2020), an SN explosion with an ejecta mass of around $10\ M_{\odot}$ could be achieved if a part of the progenitor forms a black hole.

The "precursor" of SN 2023aew is as bright as a typical Type II SN. Thus, it is possible that the precursor itself is already an SN event, and the second peak is instead caused by a delayed energy injection at the center. If the hydrogen-rich layers in the ejecta are thin enough, the second peak caused by the delayed energy injection could be observed as a hydrogen-poor event. The delayed energy injection may be caused by a fallback accretion disk toward the central compact remnant (e.g., Moriya et al. 2019; Chen et al. 2024). Depending on the initial angular momentum, the formation of the accretion disk that can provide the central energy injection could be delayed. The delayed energy input may also be caused by a delayed phase transition of neutron stars to quark stars (Ouyed et al. 2013).

5. Summary and Conclusions

In summary, SN 2023aew shows an unprecedented double-bumped light curve with two bright peaks separated by as much as 112 days. The light curve shares some similarities with the light curves of 2009ip-like SNe with their long-lived

precursors, but SN 2023aew is spectrally a stripped-envelope supernova during its main peak. SN 2023aew has a luminous 100 days long precursor, which has a 20 days rise and a spectrum similar to Type IIb SNe with a velocity of $\sim$11,800 km s^{-1}. Such a precursor is predicted by semianalytical eruption models of Matsumoto & Metzger (2022) for 2009 ip-like SNe. After 100 days, SN 2023aew brightens rapidly to -18.8 mag and exhibits a broader than typical (for SESNe) main peak with undulations in its decline. The bolometric light curves when fitted with the Arnett model for radioactivity power result in unreasonably high ^{56}Ni masses, indicating the need for an additional powering source to explain the luminosity and broadness. During the main peak phase, the SN is spectrally similar to an SN Ibc, although with weaker He I features and hydrogen, which emerges again in the nebular phase. Photospheric and nebular phase line strengths are more similar to those of SNe Ib than SNe Ic. The line strength of the nebular Hα/[N II] complex is much higher and the line width is much smaller than expected for a normal hydrogen-free SN Ibc, strengthening the case for hydrogen being present in the late spectra. Additionally, the nebular lines ([O I, [Ca II]], Mg I], and Hα) show double-peaked or "horned" profiles with one peak at rest wavelength and the other blueshifted by $\sim$1500 km s^{-1}, indicating a nonspherical geometry.

We explored the possibility of SN 2023aew being two coincident SNe in the same host galaxy and found this to be highly unlikely. We then discussed the possible origins of SN 2023aew. Although the first peak has properties consistent with an SESN (SN IIb), the dramatic rebrightening would require either a strong delayed interaction with CSM (but no signs of this interaction are seen in the spectra) or a very delayed energy injection by a central engine. The first peak could instead be an eruptive precursor to the SN explosion (second peak), additionally powering the second peak through shock interaction but with spectral signatures of interaction hidden due to asymmetric geometry. Ultimately, the powering mechanism(s) of this double-bumped supernova remain elusive. In any case, SN 2023aew and similar SNe provide a unique opportunity to study the final throes of a dying stripped massive star and we encourage further studies with detailed theoretical modeling of the data to understand its progenitor scenario.

Acknowledgments

Based on observations obtained with the Samuel Oschin Telescope 48 inch and the 60 inch Telescope at the Palomar Observatory as part of the Zwicky Transient Facility project. ZTF is supported by the National Science Foundation under grants No. AST-2034437 and a collaboration including current partners Caltech, IPAC, the Oskar Klein Center at Stockholm University, the University of Maryland, University of California, Berkeley, the University of Wisconsin at Milwaukee, University of Warwick, Ruhr University, Cornell University, Northwestern University and Drexel University. Operations are conducted by COO, IPAC, and UW. The ZTF forced photometry service was funded under the Heising-Simons Foundation grant #12540303 (PI: Graham). The Gordon and Betty Moore Foundation, through both the Data-Driven Investigator Program and a dedicated grant, provided critical funding for SkyPortal. The Oskar Klein Centre was funded by the Swedish Research Council. Partially based on observations made with the Nordic Optical Telescope, operated by the Nordic Optical Telescope Scientific Association at the Observatorio del Roque de los Muchachos, La Palma, Spain, of the Instituto de Astrofisica de Canarias. Some of the data presented here were obtained with ALFOSC. Some of the data presented herein were obtained at the W. M. Keck Observatory, which is operated as a scientific partnership among the California Institute of Technology, the University of California, and NASA; the observatory was made possible by the generous financial support of the W. M. Keck Foundation. The SED Machine is based upon work supported by the National Science Foundation under grant No. 1106171. This work has made use of data from the Asteroid Terrestrial-impact Last Alert System (ATLAS) project. The ATLAS project is primarily funded to search for near-Earth asteroids through NASA grants NN12AR55G, 80NSSC18K0284, and 80NSSC18K1575; byproducts of the NEO search include images and catalogs from the survey area. The ATLAS science products have been made possible through the contributions of the University of Hawaii Institute for Astronomy, the Queen's University Belfast, the Space Telescope Science Institute, the South African Astronomical Observatory, and The Millennium Institute of Astrophysics (MAS), Chile. This research has made use of the NASA/IPAC Infrared Science Archive, which is funded by the National Aeronautics and Space Administration and operated by the California Institute of Technology. The Liverpool Telescope is operated on the island of La Palma by Liverpool John Moores University in the Spanish Observatorio del Roque de los Muchachos of the Instituto de Astrofisica de Canarias with financial support from the UK Science and Technology Facilities Council. We acknowledge ESA Gaia, DPAC and the Photometric Science Alerts Team (http://gsaweb.ast.cam.ac.uk/alerts). Funding for the TESS mission is provided by NASA's Science Mission directorate. This paper includes data collected by the TESS mission, which are publicly available from the Mikulski Archive for Space Telescopes (MAST). This research has made use of the Spanish Virtual Observatory (https://svo.cab.inta-csic.es) project funded by MCIN/AEI/10.13039/501100011033/ through grant PID2020-112949GB-I00.

Y. Sharma thanks the LSSTC Data Science Fellowship Program, which is funded by LSSTC, NSF Cybertraining grant #1829740, the Brinson Foundation, and the Moore Foundation; her participation in the program has benefited this work. S. Schulze, N. Rehemtulla, and A. A. Miller are supported by LBNL Subcontract NO. 7707915. The material contained in this document is based upon work supported by a National Aeronautics and Space Administration (NASA) grant or cooperative agreement. Any opinions, findings, conclusions, or recommendations expressed in this material are those of the author and do not necessarily reflect the views of NASA. This work was supported through a NASA grant awarded to the Illinois/NASA Space Grant Consortium.

`Fritz` (Duev et al. 2019; van der Walt et al. 2019; Coughlin et al. 2023; a dynamic collaborative platform for time-domain astronomy) was used in this work.

Appendix A
Photospheric Phase Line Strengths and Velocities

In an attempt to quantitatively compare spectral features of SN 2023aew with different SESN subtypes, the evolution of the absorption velocity and the pseudo-equivalent width (pEW) with phase were measured, and these are plotted for

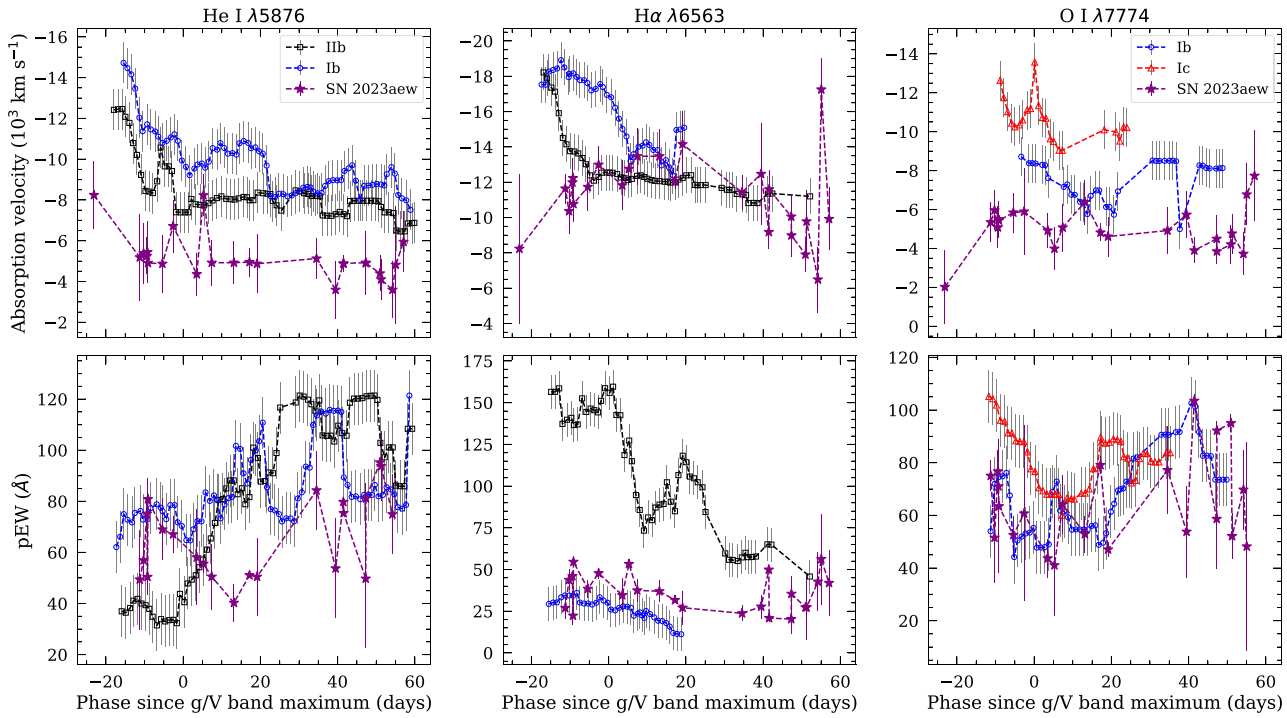

Figure 11. Evolution of absorption velocity and pseudo-equivalent width (pEW) with phase for He I λ5876, Hα, and O I λ7774. Shown for comparison are running weighted averages of velocities and pEWs for SNe IIb, Ib, and Ic with error bars of 1000 km s^{-1} and 10 Å respectively from Liu et al. (2016).

SN 2023aew along with mean values of these quantities for Types IIb, Ib, and Ic SNe as obtained from Liu et al. (2016). Running means of the absorption velocity and pEW during the photospheric phase (−20 to 60 days) for He I λ5876 and Hα for a sample of SNe IIb and Ib, and for O I λ7774 for SNe Ib and Ic are shown in Figure 11 with values for SN 2023aew (assuming the 5876 Å feature is from helium) marked as purple stars. An average error of 1000 km s^{-1} for velocities and 10 Å for pEW is shown instead of the exact errors from Liu et al. (2016). Similar to Liu et al. (2016), absorption velocities were estimated by fitting a smooth curve to the line absorption to find the minimum flux. For the pEWs, a local (pseudo-) continuum was estimated by fitting a low-order polynomial curve to points around maxima on either side of the absorption line, which was then used to estimate the equivalent width. To estimate the uncertainty on the velocity and pEW, a median filter was applied to each spectrum and the smoothened spectrum was subtracted from the original to get residuals, then the standard deviation of these residuals was taken as the flux uncertainty for each wavelength bin of the spectrum. Assuming the flux uncertainty as the 1σ noise, which obeys a Gaussian distribution centered around the smoothened spectrum, 10,000 samples were drawn to generate synthetic spectra and the line parameters were calculated on these spectra, the standard deviations of which were taken as the 1σ errors. The phases plotted for SN 2023aew (Figure 11) are not with respect to the explosion epoch but with respect to the second peak maximum (132 days from explosion) to match with the data of Liu et al. (2016).

Looking at the He I λ5876 and the Hα "feature" (as marked in Figure 6) absorption velocities with respect to phase in the upper left and middle panels of Figure 11, SN 2023aew has lower velocities at all phases than both SNe Ib and IIb. The helium velocity is roughly constant with phase at 5000 km s^{-1}. The trend observed in pEW (lower left and middle panels in Figure 11) is more indicative of SN 2023aew being similar to SNe Ib rather than to SNe IIb for both lines. The Hα strength is slightly more than visible in an SN Ib but much lower than for an average SN IIb, making SN 2023aew an intermediate, somewhat peculiar object between the two classes in this regard. The helium pEW is higher in SNe Ib before maximum and thereafter similar in both SNe Ib and IIb (Liu et al. 2016; Fremling et al. 2018), and SN 2023aew aligns more closely with SNe Ib in Figure 11. Looking at the rightmost upper and lower panels, both the O I λ7774 velocity and pEW are more similar to those of SNe Ib than to SNe Ic at all epochs. Even though SN template-matching programs estimate SN 2023aew to be a Type Ic at these epochs, the oxygen line strength for this SN is closer to those seen in SNe IIb/Ib and velocities are lower than for a typical SN Ic.

Appendix B
Note Added in Proof

At submission of this paper, another investigation of the same object was submitted to arXiv. Kangas et al. (2024) also present a comprehensive observational campaign on SN 2023aew, and although we do not agree on all details in the analysis there is overall agreement that this is an enigmatic unique object for which it is very difficult to determine the powering mechanism of the two peaks.

Appendix C
Photometry Tables

All photometric observations presented in this paper are provided in this Appendix. TESS data is presented in Table 3, Swift UVOT data in Table 4, Swift XRT data in Table 5 and all optical photometric data in Table 6.

Table 3
Log of TESS-Red Band Observations of 3σ Significance

MJD	Brightness (mag)
59941.177	19.78 ± 0.15
...	

(This table is available in its entirety in machine-readable form.)

Table 4
Log of UVOT Observations of 3σ Significance

MJD	Filter	Brightness (mag)
60076.47	uvw2	20.96 ± 0.24
...		

(This table is available in its entirety in machine-readable form.)

Table 5
Log of XRT Observations

MJD	Count rate (10^{-3} s^{-1})	F (0.3–10 keV) (10^{-13} erg s^{-1} cm^{-2})	L (0.3−10 keV) (10^{42} erg s^{-1} cm^{-2})
Individual epochs			
60076.47 ± 0.01	<5.5	<2.10	<0.30
60077.67 ± 0.33	<22.0	<8.41	<1.20
60079.71 ± 0.27	<4.4	<1.67	<0.24
60081.85 ± 0.04	<5.4	<2.08	<0.30
60083.61 ± 0.60	<10.5	<4.01	<0.57
60085.34 ± 0.14	<16.4	<6.25	<0.89
Stacking			
60080.97 ± 4.51	<1.4	<0.55	<0.08

Note. The time of reference is MJD = 60076.465219. The time reports the mid-time of the observation, and its error indicates the extent of the time bin.

Table 6
Log of Optical Photometry of 5σ Significance

MJD	Filter	Telescope	Brightness (mag)
59969.51	g	P48:ZTF	19.1 ± 0.05
...			

(This table is available in its entirety in machine-readable form.)

ORCID iDs

Yashvi Sharma https://orcid.org/0000-0003-4531-1745
Jesper Sollerman https://orcid.org/0000-0003-1546-6615
Shrinivas R. Kulkarni https://orcid.org/0000-0001-5390-8563
Takashi J. Moriya https://orcid.org/0000-0003-1169-1954
Steve Schulze https://orcid.org/0000-0001-6797-1889
Stan Barmentloo https://orcid.org/0000-0003-4800-2737
Michael Fausnaugh https://orcid.org/0000-0002-9113-7162
Avishay Gal-Yam https://orcid.org/0000-0002-3653-5598
Anders Jerkstrand https://orcid.org/0000-0001-8005-4030
Tomás Ahumada https://orcid.org/0000-0002-2184-6430
Eric C. Bellm https://orcid.org/0000-0001-8018-5348
Kaustav K. Das https://orcid.org/0000-0001-8372-997X
Christoffer Fremling https://orcid.org/0000-0002-4223-103X
Saarah Hall https://orcid.org/0000-0002-3841-380X
K. R. Hinds https://orcid.org/0000-0002-0129-806X
Theophile Jegou du Laz https://orcid.org/0009-0003-6181-4526
Viraj Karambelkar https://orcid.org/0000-0003-2758-159X
Mansi M. Kasliwal https://orcid.org/0000-0002-5619-4938
Frank J. Masci https://orcid.org/0000-0002-8532-9395
Adam A. Miller https://orcid.org/0000-0001-9515-478X
Guy Nir https://orcid.org/0000-0002-7501-5579
Daniel A. Perley https://orcid.org/0000-0001-8472-1996
Josiah N. Purdum https://orcid.org/0000-0003-1227-3738
Yu-Jing Qin https://orcid.org/0000-0003-3658-6026
Nabeel Rehemtulla https://orcid.org/0000-0002-5683-2389
R. Michael Rich https://orcid.org/0000-0003-0427-8387
Reed L. Riddle https://orcid.org/0000-0002-0387-370X
Antonio C. Rodriguez https://orcid.org/0000-0003-4189-9668
Sam Rose https://orcid.org/0000-0003-4725-4481
Jean Somalwar https://orcid.org/0000-0001-8426-5732
Jacob L. Wise https://orcid.org/0000-0003-0733-2916
Avery Wold https://orcid.org/0000-0002-9998-6732
Lin Yan https://orcid.org/0000-0003-1710-9339
Yuhan Yao https://orcid.org/0000-0001-6747-8509

References

Arcavi, I., Gal-Yam, A., Yaron, O., et al. 2011, ApJL, 742, L18
Arnett, W. D. 1982, ApJ, 253, 785
Barbarino, C., Sollerman, J., Taddia, F., et al. 2021, A&A, 651, A81
Barbary, K. 2016, extinction v0.3.0, Zenodo, doi:10.5281/zenodo.804967
Barbon, R., Benetti, S., Cappellaro, E., et al. 1995, A&AS, 110, 513
Barmentloo, S., Jerkstrand, A., Iwamoto, K., et al. 2024, arXiv:2403.08911
Bellm, E. C., Kulkarni, S. R., Barlow, T., et al. 2019, PASP, 131, 068003
Ben-Ami, S., Konidaris, N., Quimby, R., et al. 2012, Proc. SPIE, 8446, 844686
Benson, P. J., Herbst, W., Salzer, J. J., et al. 1994, AJ, 107, 1453
Bianco, F. B., Modjaz, M., Hicken, M., et al. 2014, ApJS, 213, 19
Blagorodnova, N., Neill, J. D., Walters, R., et al. 2018, PASP, 130, 035003
Blondin, S., & Tonry, J. L. 2007, ApJ, 666, 1024
Branch, D., Benetti, S., Kasen, D., et al. 2002, ApJ, 566, 1005
Breeveld, A. A., Landsman, W., Holland, S. T., et al. 2011, in AIP Conf. Proc. 1358, GAMMA RAY BURSTS 2010, ed. J. E. McEnery, J. L. Racusin, & N. Gehrels (Melville, NY: AIP), 373
Brennan, S. J., Sollerman, J., Irani, I., et al. 2024, A&A, 684, L18
Brown, P. J., Holland, S. T., Immler, S., et al. 2009, AJ, 137, 4517
Brown, P. J., Roming, P. W. A., & Milne, P. A. 2015, JHEAp, 7, 111
Burrows, D. N., Hill, J. E., Nousek, J. A., et al. 2005, SSRv, 120, 165
Cenko, S. B., Fox, D. B., Moon, D.-S., et al. 2006, PASP, 118, 1396
Chen, J., Wang, X., Ganeshalingam, M., et al. 2014, ApJ, 790, 120
Chen, P., Gal-Yam, A., Sollerman, J., et al. 2024, Natur, 625, 253
Chen, T. W., Inserra, C., Fraser, M., et al. 2018, ApJL, 867, L31
Coughlin, M. W., Bloom, J. S., Nir, G., et al. 2023, ApJS, 267, 31
Damineli, A., Conti, P. S., & Lopes, D. F. 1997, NewA, 2, 107
Dekany, R., Smith, R. M., Riddle, R., et al. 2020, PASP, 132, 038001
Duev, D. A., Mahabal, A., Masci, F. J., et al. 2019, MNRAS, 489, 3582
Elmhamdi, A., Danziger, I. J., Branch, D., et al. 2006, A&A, 450, 305
Ergon, M., Jerkstrand, A., Sollerman, J., et al. 2015, A&A, 580, A142
Evans, P. A., Beardmore, A. P., Page, K. L., et al. 2007, A&A, 469, 379
Evans, P. A., Beardmore, A. P., Page, K. L., et al. 2009, MNRAS, 397, 1177
Fang, Q., Maeda, K., Kuncarayakti, H., Sun, F., & Gal-Yam, A. 2019, NatAs, 3, 434
Fang, Q., Maeda, K., Kuncarayakti, H., & Nagao, T. 2024, NatAs, 8, 111
Fang, Q., Maeda, K., Kuncarayakti, H., et al. 2022, ApJ, 928, 151
Fausnaugh, M. M., Vallely, P. J., Kochanek, C. S., et al. 2021, ApJ, 908, 51
Fitzpatrick, E. L. 1999, PASP, 111, 63

Folatelli, G., Contreras, C., Phillips, M. M., et al. 2006, ApJ, 641, 1039
Förster, F., Cabrera-Vives, G., Castillo-Navarrete, E., et al. 2021, AJ, 161, 242
Fremling, C., Miller, A. A., Sharma, Y., et al. 2020, ApJ, 895, 32
Fremling, C., Sollerman, J., Kasliwal, M. M., et al. 2018, A&A, 618, A37
Fremling, C., Sollerman, J., Taddia, F., et al. 2016, A&A, 593, A68
Frohmaier, C., Dimitriadis, G., Pursiainen, M., et al. 2023, TNSAN, 97, 1
Fuller, J., & Ro, S. 2018, MNRAS, 476, 1853
Galama, T. J., Vreeswijk, P. M., van Paradijs, J., et al. 1998, Natur, 395, 670
Gal-Yam, A. 2017, in Observational and Physical Classification of Supernovae , ed. A. W. Alsabti & P. Murdin (Berlin: Springer), 195
Gehrels, N., Chincarini, G., Giommi, P., et al. 2004, ApJ, 611, 1005
Goldwasser, S., Yaron, O., Sass, A., et al. 2022, TNSAN, 191, 1
Graham, M. J., Kulkarni, S. R., Bellm, E. C., et al. 2019, PASP, 131, 078001
Graham, M. L., Fremling, C., Perley, D. A., et al. 2022, MNRAS, 511, 241
Guillochon, J., Parrent, J., Kelley, L. Z., & Margutti, R. 2017, ApJ, 835, 64
Gutiérrez, C. P., Bersten, M. C., Orellana, M., et al. 2021, MNRAS, 504, 4907
HI4PI Collaboration, Ben Bekhti, N., Flöer, L., et al. 2016, A&A, 594, A116
Hiramatsu, D., Matsumoto, T., Berger, E., et al. 2024, ApJ, 964, 181
Hodgkin, S. T., Harrison, D. L., Breedt, E., et al. 2021, A&A, 652, A76
Hoogendam, W., Tucker, M., Shappee, B., et al. 2023, TNSAN, 111, 1
Howell, D. A., Sullivan, M., Perrett, K., et al. 2005, ApJ, 634, 1190
IRSA 2022, Zwicky Transient Facility Image Service, IPAC, doi:10.26131/IRSA539
Jerkstrand, A., Ergon, M., Smartt, S. J., et al. 2015, A&A, 573, A12
Kangas, T., Kuncarayakti, H., Nagao, T., et al. 2024, arXiv:2401.17423
Karamehmetoglu, E., Sollerman, J., Taddia, F., et al. 2023, A&A, 678, A87
Kasen, D., Metzger, B. D., & Bildsten, L. 2016, ApJ, 821, 36
Kashi, A., & Soker, N. 2010, ApJ, 723, 602
Kim, Y. L., Rigault, M., Neill, J. D., et al. 2022, PASP, 134, 024505
Kuncarayakti, H., Sollerman, J., Izzo, L., et al. 2023, A&A, 678, A209
Leung, S.-C., Wu, S., & Fuller, J. 2021, ApJ, 923, 41
Lipunov, V. M., Vladimirov, V. V., Gorbovskoi, E. S., et al. 2019, ARep, 63, 293
Liu, Y.-Q., Modjaz, M., Bianco, F. B., & Graur, O. 2016, ApJ, 827, 90
Lyman, J. D., Bersier, D., & James, P. A. 2014, MNRAS, 437, 3848
Maeda, K., Tanaka, M., Nomoto, K., et al. 2007, ApJ, 666, 1069
Margutti, R., Milisavljevic, D., Soderberg, A. M., et al. 2014, ApJ, 780, 21
Masci, F. J., Laher, R. R., Rusholme, B., et al. 2019, PASP, 131, 018003
Masci, F. J., Laher, R. R., Rusholme, B., et al. 2023, arXiv:2305.16279
Matheson, T., Filippenko, A. V., Ho, L. C., Barth, A. J., & Leonard, D. C. 2000, AJ, 120, 1499
Matheson, T., Filippenko, A. V., Li, W., Leonard, D. C., & Shields, J. C. 2001, AJ, 121, 1648
Matsumoto, T., & Metzger, B. D. 2022, ApJ, 936, 114
Mauerhan, J. C., Smith, N., Filippenko, A. V., et al. 2013, MNRAS, 430, 1801
Milisavljevic, D., Margutti, R., Kamble, A., et al. 2015, ApJ, 815, 120
Miller, J., & Stone, R. 1987, The CCD Cassegrain Spectrograph at the Shane Reflector Technical Report No. 48, Lick Observatory
Modjaz, M. 2007, PhD thesis, Harvard Univ.
Modjaz, M., Kirshner, R. P., Blondin, S., Challis, P., & Matheson, T. 2008, ApJL, 687, L9
Modjaz, M., Liu, Y. Q., Bianco, F. B., & Graur, O. 2016, ApJ, 832, 108
Modjaz, M., Stanek, K. Z., Garnavich, P. M., et al. 2006, ApJL, 645, L21
Moriya, T. J., Müller, B., Chan, C., Heger, A., & Blinnikov, S. I. 2019, ApJ, 880, 21
Munoz-Arancibia, A., Bauer, F. E., Pignata, G., et al. 2023, TNSTR 2023-166, 1
Nicholl 2018, mnicholl/superbol: superbol v1.0, Zenodo, doi:10.5281/zenodo.2155821
Nyholm, A., Sollerman, J., Taddia, F., et al. 2017, A&A, 605, A6
Ofek, E. O., Sullivan, M., Shaviv, N. J., et al. 2014, ApJ, 789, 104
Oke, J. B., Cohen, J. G., Carr, M., et al. 1995, PASP, 107, 375
Oke, J. B., & Gunn, J. E. 1982, PASP, 94, 586
Orellana, M., & Bersten, M. C. 2022, A&A, 667, A92
Ouyed, R., Koning, N., & Leahy, D. 2013, RAA, 13, 1463
Parrent, J. T., Milisavljevic, D., Soderberg, A. M., & Parthasarathy, M. 2016, ApJ, 820, 75
Pastorello, A., Cappellaro, E., Inserra, C., et al. 2013, ApJ, 767, 1
Patat, F., Cappellaro, E., Danziger, J., et al. 2001, ApJ, 555, 900
Perley, D. A. 2019, PASP, 131, 084503
Perley, D. A., Fremling, C., Sollerman, J., et al. 2020, ApJ, 904, 35
Phillips, M. M., & Burns, C. R. 2017, in Handbook of Supernovae, ed. A. W. Alsabti & P. Murdin (Berlin: Springer), 2543
Piascik, A. S., Steele, I. A., Bates, S. D., et al. 2014, Proc. SPIE, 9147, 91478H
Popov, D. V. 1993, ApJ, 414, 712
Prentice, S. J., Mazzali, P. A., Pian, E., et al. 2016, MNRAS, 458, 2973
Prochaska, J. X., Hennawi, J. F., Westfall, K. B., et al. 2020, JOSS, 5, 2308
Quataert, E., & Shiode, J. 2012, MNRAS, 423, L92
Rehemtulla, N., Miller, A. A., Jegou Du Laz, T., et al. 2024, arXiv:2401.15167
Renzo, M., Farmer, R., Justham, S., et al. 2020, A&A, 640, A56
Richmond, M. W., Treffers, R. R., Filippenko, A. V., & Paik, Y. 1996, AJ, 112, 732
Richmond, M. W., Treffers, R. R., Filippenko, A. V., et al. 1994, AJ, 107, 1022
Ricker, G. R. 2014, JAAVSO, 42, 234
Rigault, M., Neill, J. D., Blagorodnova, N., et al. 2019, A&A, 627, A115
Rodrigo, C., & Solano, E. 2020, in XIV.0 Scientific Meeting (virtual) of the Spanish Astronomical Society, 182
Rodrigo, C., Solano, E., & Bayo, A. 2012, SVO Filter Profile Service Version 1.0, IVOA Working Draft 15 October 2012, doi:10.5479/ADS/bib/2012ivoa.rept.1015R
Roming, P. W. A., Kennedy, T. E., Mason, K. O., et al. 2005, SSRv, 120, 95
Schlafly, E. F., & Finkbeiner, D. P. 2011, ApJ, 737, 103
Sheinis, A. I., Bolte, M., Epps, H. W., et al. 2002, PASP, 114, 851
Shingles, L., Smith, K. W., Young, D. R., et al. 2021, TNSAN, 7, 1
Shivvers, I., Filippenko, A. V., Silverman, J. M., et al. 2019, MNRAS, 482, 1545
Smith, K. W., Smartt, S. J., Young, D. R., et al. 2020, PASP, 132, 085002
Smith, N. 2011, MNRAS, 415, 2020
Soker, N. 2001, MNRAS, 325, 584
Soker, N. 2004, ApJ, 612, 1060
Soker, N., & Kashi, A. 2013, ApJL, 764, L6
Sollerman, J., Fransson, C., Barbarino, C., et al. 2020, A&A, 643, A79
Sollerman, J., Holland, S. T., Challis, P., et al. 2002, A&A, 386, 944
Sollerman, J., Kozma, C., Fransson, C., et al. 2000, ApJL, 537, L127
Sollerman, J., Yang, S., Perley, D., et al. 2022, A&A, 657, A64
Steele, I. A., Smith, R. J., Rees, P. C., et al. 2004, Proc. SPIE, 5489, 679
Stritzinger, M. D., Anderson, J. P., Contreras, C., et al. 2018, A&A, 609, A134
Strotjohann, N. L., Ofek, E. O., Gal-Yam, A., et al. 2021, ApJ, 907, 99
Taddia, F., Stritzinger, M. D., Bersten, M., et al. 2018, A&A, 609, A136
Taubenberger, S., Valenti, S., Benetti, S., et al. 2009, MNRAS, 397, 677
Tody, D. 1986, Proc. SPIE, 627, 733
Tody, D. 1993, in ASP Conf. Ser. 52, Astronomical Data Analysis Software and Systems II , ed. R. J. Hanisch, R. J. V. Brissenden, & J. Barnes (San Francisco: ASP), 173
Tominaga, N., Tanaka, M., Nomoto, K., et al. 2005, ApJL, 633, L97
Tonry, J. L., Denneau, L., Heinze, A. N., et al. 2018, PASP, 130, 064505
Tsuna, D., Matsumoto, T., Wu, S. C., & Fuller, J. 2024, arXiv:2401.02389
Valenti, S., Benetti, S., Cappellaro, E., et al. 2008a, MNRAS, 383, 1485
Valenti, S., Elias-Rosa, N., Taubenberger, S., et al. 2008b, ApJL, 673, L155
van Baal, B. F. A., Jerkstrand, A., Wongwathanarat, A., & Janka, H.-T. 2023, MNRAS, 523, 954
van der Walt, S. J., Crellin-Quick, A., & Bloom, J. S. 2019, JOSS, 4, 1247
van Driel, W., Yoshida, S., Nakada, Y., et al. 1993, PASJ, 45, L59
Wang, L., Höflich, P., & Wheeler, J. C. 1997, ApJL, 483, L29
Wilson, J. C., Henderson, C. P., Herter, T. L., et al. 2004, Proc. SPIE, 5492, 1295
Wise, J., Hinds, K., & Perley, D. 2023, TNSCR 2023-750, 1
Woosley, S. E. 2017, ApJ, 836, 244
Woosley, S. E., Blinnikov, S., & Heger, A. 2007, Natur, 450, 390
Woosley, S. E., & Heger, A. 2015, ApJ, 810, 34
Wu, S., & Fuller, J. 2021, ApJ, 906, 3
Yang, S., & Sollerman, J. 2023, ApJS, 269, 40
Yaron, O., & Gal-Yam, A. 2012, PASP, 124, 668
Yoon, S. C., Woosley, S. E., & Langer, N. 2010, ApJ, 725, 940